

A Comparison of Staggered-Mesh Lagrange Plus Remap and Cell- Centered Direct Eulerian Godunov Schemes for Eulerian Shock Hydrodynamics

R.B. Pember and R.W. Anderson

U.S. Department of Energy

Lawrence
Livermore
National
Laboratory

*This article was submitted to
Nuclear Explosives Code Developers Collaborations (NECDC) 2000
Oakland, CA
October 23-27, 2000*

November 22, 2000

DISCLAIMER

This document was prepared as an account of work sponsored by an agency of the United States Government. Neither the United States Government nor the University of California nor any of their employees, makes any warranty, express or implied, or assumes any legal liability or responsibility for the accuracy, completeness, or usefulness of any information, apparatus, product, or process disclosed, or represents that its use would not infringe privately owned rights. Reference herein to any specific commercial product, process, or service by trade name, trademark, manufacturer, or otherwise, does not necessarily constitute or imply its endorsement, recommendation, or favoring by the United States Government or the University of California. The views and opinions of authors expressed herein do not necessarily state or reflect those of the United States Government or the University of California, and shall not be used for advertising or product endorsement purposes.

This is a preprint of a paper intended for publication in a journal or proceedings. Since changes may be made before publication, this preprint is made available with the understanding that it will not be cited or reproduced without the permission of the author.

This report has been reproduced
directly from the best available copy.

Available to DOE and DOE contractors from the
Office of Scientific and Technical Information
P.O. Box 62, Oak Ridge, TN 37831
Prices available from (423) 576-8401
<http://apollo.osti.gov/bridge/>

Available to the public from the
National Technical Information Service
U.S. Department of Commerce
5285 Port Royal Rd.,
Springfield, VA 22161
<http://www.ntis.gov/>

OR

Lawrence Livermore National Laboratory
Technical Information Department's Digital Library
<http://www.llnl.gov/tid/Library.html>

A Comparison of Staggered-Mesh Lagrange Plus Remap and Cell-Centered Direct Eulerian Godunov Schemes for Eulerian Shock Hydrodynamics

Richard B. Pember, Robert W. Anderson
Lawrence Livermore National Laboratory

We present a comparison of two algorithms for solving the equations of unsteady inviscid compressible flow in an Eulerian frame. The first algorithm is a staggered grid Lagrange plus remap scheme. The Lagrange step in this method is a time-centered version of the scheme due to Tipton, while the remap step employs a variant of the corner transport upwind scheme due to Colella. The second algorithm is a spatially operator-split version of the higher-order Godunov scheme for gas dynamics due to Colella. We use the two methods to compute solutions to a number of one- and two-dimensional problems. Our results show the accuracy and performance of the two schemes to be generally equivalent. In a 1984 survey paper by Woodward and Colella, staggered grid, Lagrange plus remap, artificial viscosity schemes did not compare favorably with cell-centered direct Eulerian higher-order Godunov methods. We examine, therefore, how certain features of the staggered grid scheme discussed here contribute to its improved accuracy. We show in particular that the improved accuracy of the present scheme is due in part to the use of a monotonic artificial viscosity in the Lagrange step and the use of an improved upwind method in the remap step.

Introduction

Shock capturing methods have always played a central role in the computational modeling of compressible flows. Consequently there has always been interest in assessing the relative accuracy and performance of the various algorithms employed in the field. Sixteen years ago there appeared one such assessment in a review article by Woodward and Colella (1984). They compare three general methodologies – namely, the Godunov, the artificial viscosity, and the linear hybridization approaches – and six particular methods for modeling compressible flow in an Eulerian frame. The methods are assessed from an examination of the computational results for a series of one- and two-dimensional problems characterized by strong shocks.

The methods examined by Woodward and Colella (1984) include a direct Eulerian version of the piecewise-parabolic method (PPM), the MUSCL scheme of van Leer, and BBC, a staggered grid, Lagrange plus remap scheme with a von Neumann-Richtmyer artificial viscosity. The conclusions include a ranking of the accuracy of the schemes in which PPM is ranked first, MUSCL second, and BBC fourth. Although it was not the intent of the authors, the reader is left with an impression of the superiority of higher-order upwind methods and the inferiority of artificial viscosity schemes.

Although it has fallen out of general usage for Eulerian calculations in the intervening years, the staggered grid, artificial viscosity Lagrange plus remap approach remains important in the context of arbitrary Lagrangian-Eulerian (ALE) methods. (See papers by Benson (1992) and Hirt *et al.* (1974) for general discussions of ALE methodologies and by Darlington

et al. (1999), Peterkin *et al.* (1998), Shestakov *et al.* (2000) and Smith (1999) for recent applications.) In the setting of gas dynamics, the ALE formulation of the governing equations describes the evolution of a compressible flow on a grid moving with an arbitrary velocity. There are essentially two approaches to solving the ALE equations: an unsplit approach in which the grid motion and the evolution of the fluid are considered simultaneously, and a split approach. The split approach consists of three steps: a Lagrange step, a grid motion step in which the Lagrangian grid is modified, if necessary, to reduce grid distortion, and a remap step in which the solution at the end of the Lagrangian step is conservatively interpolated onto the modified grid via an advection scheme. See Benson (1992) and Darlington *et al.* (2000) for discussions on the relative merits of the unsplit and the split approaches.

Motivated by its importance in the context of split ALE schemes, in this paper we reexamine the comparison of the staggered grid, artificial viscosity Lagrange plus remap approach with the direct Eulerian, higher-order Godunov methodology in the context of single fluid gas dynamics. The remainder of the paper will be organized as follows.

After briefly reviewing the equations of gas dynamics, we formulate and discuss the staggered grid Lagrange plus remap scheme. The Lagrange step uses a standard approach, namely, a predictor-corrector formulation in which the flow variables are not staggered in time and which otherwise follows the scheme due to Tipton (1990). In particular, it employs the spatial discretization of HEMP (Wilkins, 1964; Wilkins 1999), a multidimensional extension of the scalar monotonic artificial viscosity due to Christensen (1990), and a momentum conserving variation of the simple kinematic hourglass filter due to Margolin and Pyun (1987). The advection step uses a variation of the corner transport upwind method of Colella (1990) as formulated for moving quadrilateral grids (Bell *et al.*, 1989). (Jun (2000) has applied the corner transport upwind scheme in a remap step as well.)

We next review the second algorithm, a spatially split version of the higher-order Godunov scheme due to Colella (Colella *et al.*, 1993; Pember *et al.*, 1996; Miller and Puckett, 1996). This method employs piecewise linear cell profiles which use a fourth-order approximation to the spatial derivatives (Colella, 1985), an approximate Riemann solver, and two additional dissipation mechanisms, a Lapidus artificial viscosity and a slope flattening technique (Colella and Woodward, 1984). The approximate Riemann solver is a linearized Riemann solver (Roe, 1981) with a special treatment for rarefactions (Colella *et al.*, 1993; Colella and Puckett, 1997).

We then use the two methods to compute solutions to a number of one- and two-dimensional problems. (We will refer to the two methods as the Lagrange plus remap scheme and the higher-order Godunov scheme.) Our test problems include two of the problems examined by Woodward and Colella (1984), the interacting blast wave and the double Mach reflection of a strong shock. We also examine a number of additional problems, namely, the planar Noh problem, the cylindrical Sedov problem, a refraction of an oblique shock at a density interface, and the LeBlanc shock tube. Our results demonstrate that the accuracy of the two schemes is generally equivalent, each scheme displaying both relative strengths and weaknesses. The results show in particular that the improved accuracy of the present Lagrange plus remap scheme relative to BBC is due in part to the use of an improved artificial viscosity in the Lagrange step and an improved upwind method in the remap step.

Governing equations

The equations of single fluid gas dynamics can be expressed in either of two equivalent formulations, the conservative and the material derivative forms. In two dimensional rectangular coordinates, the conservative formulation of the equations is

$$\frac{\partial U}{\partial t} + \frac{\partial F(U)}{\partial x} + \frac{\partial G(U)}{\partial y} = 0 \quad (1)$$

where

$$U = \begin{pmatrix} \rho \\ \rho u \\ \rho v \\ \rho E \end{pmatrix}, \quad F(U) = \begin{pmatrix} \rho u \\ \rho u^2 + p \\ \rho uv \\ \rho uE + pu \end{pmatrix}, \quad G(U) = \begin{pmatrix} \rho v \\ \rho uv \\ \rho v^2 + p \\ \rho vE + pv \end{pmatrix},$$

and $E = 1/2(u^2 + v^2) + e$. The corresponding material derivative formulation is

$$\frac{D\rho}{Dt} = -\rho \nabla \cdot U \quad (2)$$

$$\rho \frac{DU}{Dt} = -\nabla p \quad (3)$$

$$\frac{De}{Dt} = -\frac{p}{\rho} \nabla \cdot U = -\frac{D}{Dt} \left(\frac{1}{\rho} \right) p \quad (4)$$

where $U = (u, v)^T$. In either formulation, p is defined by the equation of state $p = p(\rho, e)$. For all examples considered in this paper, p is given by the polytropic equation of state $p = (\gamma - 1) \rho e$.

Lagrange Plus Remap Scheme

In this section we present the Lagrange plus remap scheme for solving the material derivative formulation of the Euler equations, (2)-(4), in two-dimensional rectangular coordinates. The method is an operator split scheme in that it consists of two distinct steps, the Lagrange step and the remap step. During a single time step the equations of gas dynamics are first advanced to the new time on a grid that moves with the fluid. The solution on this grid is then remapped via an advection over a pseudo-timestep during which the grid returns to its original configuration.

We solve the equations on a structured grid of quadrilateral cells. The flow variables are staggered: ρ and e are cell-centered quantities while $U = (u, v)$ is node-centered. The grid itself is defined by the positions $X = (x, y)$ of the nodes. V denotes the cell area; see Figure 1. We use the following indexing convention. The cells themselves are indexed as i, j , the four nodes as $i \pm 1/2, j \pm 1/2$, and the four bounding faces as $i \pm 1/2, j$ and $i, j \pm 1/2$.

Let $L_{Lag}^{\Delta t}$ and L_{remap} denote the numerical solution operators for the Lagrange and the remap steps. (Note that there is no time increment associated with the remap step.) The overall method used to advance the numerical solution U^n from time t^n to $t^{n+1} = t^n + \Delta t^n$ is then

$$U^{n+1} = L_{remap} L_{Lag}^{\Delta t^n} U^n.$$

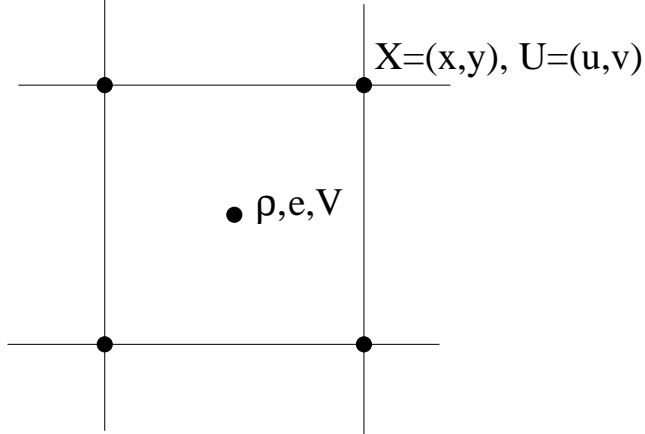


Figure 1: Staggered grid representation of the flow variables.

The stability restriction on the numerical method is a cumulative restriction resulting from an application of the Courant-Friedrichs-Lewy (CFL) condition in each sweep, i.e.,

$$\Delta t^n = \min \left(\Delta t_{Lag}^n, \Delta t_{remap}^n \right),$$

where

$$\Delta t_{Lag}^n = \sigma \min_{i,j} \frac{l_{ij}}{c_{i,j}^n}, \quad \Delta t_{remap}^n = \sigma \min_{i,j} \frac{l_{i,j}}{\max |U_{i\pm 1/2, j\pm 1/2}^n|}, \quad (5)$$

l_{ij} is a measure of the shortest distance across cell ij , c is the sound speed, and the CFL number σ is a positive constant, $\sigma < 1$. (Note that even though there is no time step associated with the remap step, it still imposes a restriction on the maximum size of Δt^n . The restriction $\Delta t^n \leq \Delta t_{remap}^n$ is equivalent to the restriction that each cell at the end of the Lagrange step have some intersection with itself in the original grid. This restriction can be relaxed with subcycling of the remap step.)

Although the overall method is a fractional step scheme, we note that it is unnecessary to use Strang splitting (Crandall and Majda, 1980; Strang, 1968) (i.e., to alternate the order of the Lagrange and remap steps) to achieve second order accuracy because the remap step can simply be considered an interpolation from the grid at the end of the Lagrange step onto the original grid.

We now describe each of the two steps in more detail. The Lagrange step uses a predictor-corrector formulation in which the flow variables are not staggered in time and which otherwise follows the scheme due to Tipton (1990). The scheme uses a multidimensional form of the scalar monotonic artificial viscosity due to Christensen (1990). In this approach, the artificial viscosity q is a cell-centered quantity that acts in the same manner as pressure. In one space dimension, this viscosity is given by

$$q_i = \begin{cases} \rho_i |\Delta u_i| (c_Q |\Delta u_i| (1 - \phi^2) + c_L c_i (1 - \phi)) & \Delta u_i < 0 \\ 0 & \text{otherwise} \end{cases} \quad (6)$$

where $\Delta u_i = u_{i+1/2} - u_{i-1/2}$ and

$$\phi_i = \max(0, \min(1, 2R_{i+1}, 2R_{i-1}, .5(R_{i+1} + R_{i-1}))),$$

where $R_{i\pm 1} = \Delta u_{i\pm 1} / \Delta u_i$. When $\phi = 0$, the viscosity reduces to the viscosity due to Landshoff (1955) and Noh (1956), often called the standard Lagrange viscosity. c_Q and c_L are constants that are generally set to $.25(\gamma + 1)$ and $.5$ for polytropic gases (Benson, 1992). The effect of the limiters $1 - \phi$ and $1 - \phi^2$ is to reduce the viscosity in regions with moderate velocity gradients, and thereby reduce the numerical diffusion of the scheme. We refer the reader to Wilkins (1999) for one extension of this viscosity to multiple dimensions.

A momentum conserving variation of the simple kinematic hourglass filter presented by Margolin and Pyun (1987) is also employed to remove hourglass modes from the velocity field. The use of the hourglass filter to modify the velocity in turn requires that the internal energy update account for the loss of kinetic energy in the application of the filter. The use of an hourglass filter and an artificial viscosity imply that we effectively solve modified forms of the momentum and energy equations,

$$\rho \frac{DU}{Dt} = -\nabla(p + q) + \rho a_{HG} \quad (7)$$

$$\frac{De}{Dt} = -\frac{p + q}{\rho} \nabla \cdot U + \dot{e}_{HG} = -\frac{D}{Dt} \left(\frac{1}{\rho} \right) (p + q) + \dot{e}_{HG}, \quad (8)$$

where a_{HG} and \dot{e}_{HG} refer to the acceleration and the heating due to the hourglass filter. a_{HG} is defined so that the integral of ρa_{HG} over the computational domain is zero.

The Lagrange step also uses the spatial discretization of HEMP (Wilkins, 1964; Wilkins, 1999). For gas dynamics, this primarily effects the definition of the mass of a node and of the control volume used to formulate a conservative differencing scheme for momentum. Figure 2 shows four computational cells – A, B, C, D – and the nine nodes associated with them. In the HEMP discretization, the mass of node 0 is defined by

$$m_0 = (\rho_A V_A + \rho_B V_B + \rho_C V_C + \rho_D V_D) / 2,$$

and the associated force control volume is defined as the quadrilateral $\overline{1357}$ (Wilkins, 1964; Wilkins, 1999). (We use the notation $\overline{p_1 p_2 \dots p_n}$ to denote the n -gon with vertices p_1, p_2, \dots, p_n for $n \geq 3$. For $n = 2$, we use it to denote a line segment.) This choice of mass and force control volume would seemingly result in a non-conservative discretization of the momentum equation. The reason why the discretization is nevertheless conservative is that an equivalent control volume is the octagon $\overline{abcdefgh}$, where $b, d, f,$ and h are the midpoints of segments $\overline{50}, \overline{70}, \overline{03},$ and $\overline{01}$, and $a, c, e,$ and g are points interior to cells $A, B, C,$ and D . The corresponding mass for this control volume is

$$\tilde{m}_0 = (\rho_A V_A + \rho_B V_B + \rho_C V_C + \rho_D V_D) / 4. \quad (9)$$

By Green's theorem,

$$\int_{\overline{abcdefgh}} \nabla(p + q) dV = \int_{\partial(\overline{abcdefgh})} (p + q) \mathbf{n} ds,$$

where \mathbf{n} is the outward facing normal and dV and ds are the standard area and length measures. HEMP uses constant pressure elements, i.e., the pressure is assumed to be constant in each cell. Using the fact that $\int \mathbf{n} ds = 0$ over a closed curve, we see that

$$\int_{\partial(\overline{abcdefgh})} (p + q) \mathbf{n} ds = \int_{\partial(\overline{bdfh})} (p + q) \mathbf{n} ds.$$

The semi-discrete form of the velocity update is then given by

$$\tilde{m}_0 \frac{DU}{Dt} = \int_{\partial(\overline{bdfh})} (p + q) \mathbf{n} ds + \tilde{m}_0 a_{HG}.$$

Multiplying both sides by two, we obtain the usual semi-discrete form of the HEMP momentum update:

$$m_0 \frac{DU}{Dt} = \int_{\partial(\overline{1357})} (p + q) \mathbf{n} ds + m_0 a_{HG},$$

or

$$\frac{DU}{Dt} = a \equiv \frac{1}{m_0} \left(\int_{\partial(\overline{1357})} (p + q) \mathbf{n} ds \right) + a_{HG}. \quad (10)$$

We note that given (9), the cell-centered kinetic and total energy are defined by

$$ke_{ij} = \frac{1}{4} \sum_{\text{nodes of } ij} \frac{1}{2} (u^2 + v^2) \quad \text{and} \quad E_{ij} = e_{ij} + ke_{ij},$$

respectively.

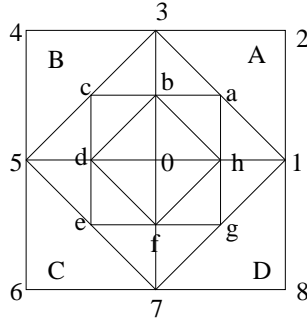


Figure 2: Derivation of control volume for node 0.

The Heun (modified trapezoidal) method is used as the basic predictor-corrector scheme to solve equations (2), (7), and (8). In the predictor, we compute predicted values of ρ, U, e, X , and V at time $n + 1$. In the corrector, we use the predicted values to form time-centered source terms with which we compute the solution at time n . We use the superscript $n + 1, p$ to denote the predicted values. The predictor-corrector scheme has the following steps:

1. Compute a^n using time n values and equation (10).
2. Compute the predicted velocity:

$$U_{i+\frac{1}{2},j+\frac{1}{2}}^{n+1,p} = U_{i+\frac{1}{2},j+\frac{1}{2}}^n + \Delta t a_{i+\frac{1}{2},j+\frac{1}{2}}^n.$$

3. Compute the predicted node positions:

$$X_{i+\frac{1}{2},j+\frac{1}{2}}^{n+1,p} = X_{i+\frac{1}{2},j+\frac{1}{2}}^n + .5\Delta t \left(U_{i+\frac{1}{2},j+\frac{1}{2}}^n + U_{i+\frac{1}{2},j+\frac{1}{2}}^{n+1,p} \right).$$

4. Compute the predicted zone volumes $V_{ij}^{n+1,p}$.

5. Compute the predicted densities:

$$\rho_{ij}^{n+1,p} = \rho_{ij}^n V_{ij}^n / V_{ij}^{n+1,p}.$$

6. Compute the predicted internal energy

$$e_{ij}^{n+1,p} = e_{ij}^n - (p_{ij}^n + q_{ij}^n) \left(1/\rho_{ij}^{n+1,p} - 1/\rho_{IJ}^n \right) + \Delta t \dot{e}_{HG,ij}^n.$$

7. Compute $a^{n+1,p}$ using time n values for q , predicted values for other quantities, and equation (10).

8. Compute the new velocity:

$$U_{i+\frac{1}{2},j+\frac{1}{2}}^{n+1} = U_{i+\frac{1}{2},j+\frac{1}{2}}^n + .5\Delta t \left(a_{i+\frac{1}{2},j+\frac{1}{2}}^n + a_{i+\frac{1}{2},j+\frac{1}{2}}^{n+1,p} \right).$$

9. Compute the new node positions:

$$X_{i+\frac{1}{2},j+\frac{1}{2}}^{n+1} = X_{i+\frac{1}{2},j+\frac{1}{2}}^n + .5\Delta t \left(U_{i+\frac{1}{2},j+\frac{1}{2}}^n + U_{i+\frac{1}{2},j+\frac{1}{2}}^{n+1} \right).$$

10. Compute the new zone volumes V_{ij}^{n+1} .

11. Compute the new densities:

$$\rho_{ij}^{n+1} = \rho_{ij}^n V_{ij}^n / V_{ij}^{n+1}.$$

12. Compute the new internal energy

$$e_{ij}^{n+1} = e_{ij}^n - \left(q_{ij}^n + .5 \left(p_{ij}^n + p_{ij}^{n+1,p} \right) \right) \left(1/\rho_{ij}^{n+1} - 1/\rho_{IJ}^n \right) + .5\Delta t \left(\dot{e}_{HG,ij}^n + \dot{e}_{HG,ij}^{n+1,p} \right).$$

In the remap step we use a conservative advection scheme to interpolate the solution obtained above from the grid defined by X^{n+1} onto the original grid defined by X^n . We formulate this interpolation as an initial value problem in which we solve

$$\partial w / \partial \tau = 0 \tag{11}$$

on a moving grid. w and τ denote an arbitrary scalar quantity defined on the grid and a pseudo-time, respectively. At $\tau = 0$, w is defined by its value at the end of the Lagrange step. We integrate (11) from $\tau = 0$ to $\tau = \tau_f$. Over this time, the grid moves from $\mathbf{x}^{old} = X^{n+1}$ to $\mathbf{x}^{new} = X^n$. The grid velocity is defined by $\mathbf{s} = (\mathbf{x}^{new} - \mathbf{x}^{old}) / \tau_f$. We now transform (11) to index space coordinates $(\xi, \eta) = (i, j)$ and thereby obtain the equation

$$\frac{\partial Jw}{\partial \tau} - \frac{\partial}{\partial \xi} \left(\mathbf{n}^\xi \cdot \mathbf{s}w \right) - \frac{\partial}{\partial \eta} \left(\mathbf{n}^\eta \cdot \mathbf{s}w \right) = 0 \tag{12}$$

where

$$J = x_\xi y_\eta - y_\xi x_\eta, \quad \mathbf{n}^\xi = (y_\eta, -x_\eta), \quad \mathbf{n}^\eta = (-y_\xi, x_\xi).$$

We now solve (12) with a conservative difference scheme.

In order to ensure freestream preservation the fluxes used in the conservative difference scheme must be formulated as products of edge values and either transport volumes (in the case of density) or transport masses (in the case of all other quantities) (Benson, 1992a). The transport volume associated with an edge is the signed quadrilateral formed by the old and the new edges. In Figure 3, the arrows point from the old grid to the new grid. A, B, G, and H represent positive transport volumes while C, D, E, and F represent negative ones. More precisely, transport volumes $\delta\sigma$ are defined by

$$\begin{aligned} \delta\sigma_{i+\frac{1}{2},j} &= .5 \left((x_{i+\frac{1}{2},j+\frac{1}{2}}^{old} - x_{i+\frac{1}{2},j-\frac{1}{2}}^{new})(y_{i+\frac{1}{2},j-\frac{1}{2}}^{old} - y_{i+\frac{1}{2},j+\frac{1}{2}}^{new}) - \right. \\ &\quad \left. (x_{i+\frac{1}{2},j-\frac{1}{2}}^{old} - x_{i+\frac{1}{2},j+\frac{1}{2}}^{new})(y_{i+\frac{1}{2},j+\frac{1}{2}}^{old} - y_{i+\frac{1}{2},j-\frac{1}{2}}^{new}) \right) \\ \delta\sigma_{i,j+\frac{1}{2}} &= .5 \left((x_{i-\frac{1}{2},j+\frac{1}{2}}^{new} - x_{i+\frac{1}{2},j+\frac{1}{2}}^{old})(y_{i-\frac{1}{2},j+\frac{1}{2}}^{old} - y_{i+\frac{1}{2},j+\frac{1}{2}}^{new}) - \right. \\ &\quad \left. (x_{i-\frac{1}{2},j+\frac{1}{2}}^{old} - x_{i+\frac{1}{2},j+\frac{1}{2}}^{new})(y_{i-\frac{1}{2},j+\frac{1}{2}}^{old} - y_{i+\frac{1}{2},j+\frac{1}{2}}^{new}) \right). \end{aligned}$$

Volume fluxes are then defined by $F_{i+\frac{1}{2},j} = -\delta\sigma_{i+\frac{1}{2},j}$ and $F_{i,j+\frac{1}{2}} = -\delta\sigma_{i,j+\frac{1}{2}}$, i.e.,

$$V_{ij}^{new} = V_{ij}^{old} + (F_{i-\frac{1}{2},j} - F_{i+\frac{1}{2},j}) + (F_{i,j-\frac{1}{2}} - F_{i,j+\frac{1}{2}}).$$

Transport masses for cell-centered quantities can be defined by the product of the density and the transport volume at an edge:

$$\delta m_{i+\frac{1}{2},j} = \rho_{i+\frac{1}{2},j} \delta\sigma_{i+\frac{1}{2},j}, \quad \delta m_{i,j+\frac{1}{2}} = \rho_{i,j+\frac{1}{2}} \delta\sigma_{i,j+\frac{1}{2}}. \quad (13)$$

Mass fluxes are defined by $F_{i+\frac{1}{2},j} = -\delta m_{i+\frac{1}{2},j}$ and $F_{i,j+\frac{1}{2}} = -\delta m_{i,j+\frac{1}{2}}$, i.e.,

$$m_{ij}^{new} = m_{ij}^{old} + (F_{i-\frac{1}{2},j} - F_{i+\frac{1}{2},j}) + (F_{i,j-\frac{1}{2}} - F_{i,j+\frac{1}{2}}),$$

where $m_{ij} = \rho_{ij} V_{ij}$ is the mass of cell ij .

The control volume for momentum remap is considered a logical rectangle; for node 0 in Figure 2, the control volume is $acef$. The four bounding faces of the control volume associated with the node at $(i + \frac{1}{2}, j + \frac{1}{2})$ are indexed as $(i, j + \frac{1}{2})$, $(i + 1, j + \frac{1}{2})$, $(i + \frac{1}{2}, j)$, and $(i + \frac{1}{2}, j + 1)$. The transport masses for these faces are given by

$$\begin{aligned} \delta m_{i+\frac{1}{2},j}^{nodal} &= \frac{1}{4} \left(\delta m_{i,j+\frac{1}{2}} + \delta m_{i+1,j+\frac{1}{2}} + \delta m_{i,j-\frac{1}{2}} + \delta m_{i+1,j-\frac{1}{2}} \right) \\ \delta m_{i,j+\frac{1}{2}}^{nodal} &= \frac{1}{4} \left(\delta m_{i+\frac{1}{2},j} + \delta m_{i+\frac{1}{2},j+1} + \delta m_{i-\frac{1}{2},j} + \delta m_{i-\frac{1}{2},j+1} \right). \end{aligned} \quad (14)$$

These definitions of transport mass are necessary for freestream preservation of velocity given the definition of nodal mass (9) in the HEMP discretization.

The remap algorithm can now be summarized as follows:

1. Compute transport volumes at all edges.
2. Compute densities at all edges.

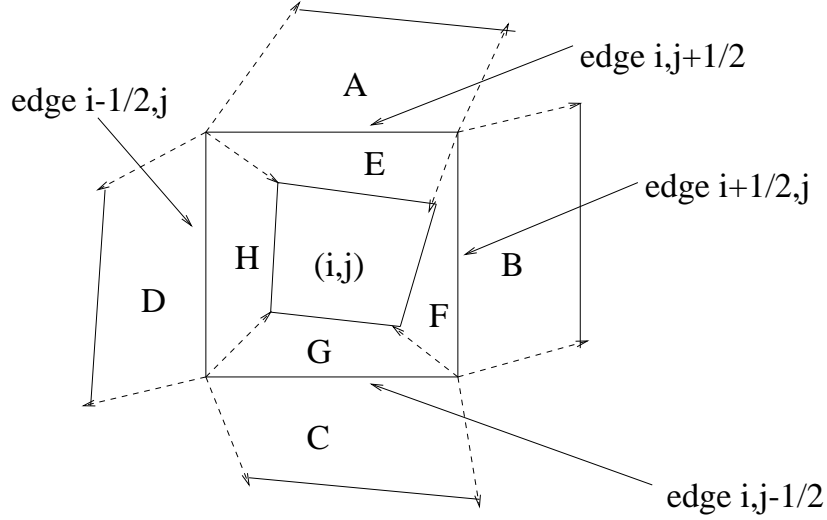


Figure 3: Illustration of transport volumes.

3. Compute transport masses using (13) and (14).
4. Remap density by

$$V_{ij}^{new} \rho_{ij}^{new} = V_{ij}^{old} \rho_{ij}^{old} + (F_{i-1/2,j} - F_{i+1/2,j}) + (F_{i,j-1/2} - F_{i,j+1/2})$$

where

$$F_{i+1/2,j} = -\rho_{i+1/2,j} \delta \sigma_{i+1/2,j}, \quad F_{i,j+1/2} = -\rho_{i,j+1/2} \delta \sigma_{i,j+1/2}.$$

5. Remap $w = u, v$ by

$$m_{i+1/2,j+1/2}^{new} w_{i+1/2,j+1/2}^{new} = m_{i+1/2,j+1/2}^{old} w_{i+1/2,j+1/2}^{old} + (F_{i,j+1/2} - F_{i+1,j+1/2}) + (F_{i+1/2,j} - F_{i+1/2,j+1})$$

where

$$F_{i,j+1/2} = -w_{i,j+1/2} \delta m_{i,j+1/2}^{nodal}, \quad F_{i+1/2,j} = -w_{i+1/2,j} \delta m_{i+1/2,j}^{nodal}.$$

6. Remap $w = ke, e$ by

$$m_{ij}^{new} w_{ij}^{new} = m_{ij}^{old} w_{ij}^{old} + (F_{i-1/2,j} - F_{i+1/2,j}) + (F_{i,j-1/2} - F_{i,j+1/2})$$

where

$$F_{i+1/2,j} = -w_{i+1/2,j} \delta m_{i+1/2,j}, \quad F_{i,j+1/2} = -w_{i,j+1/2} \delta m_{i,j+1/2}.$$

7. Enforce conservation of total energy by

$$e_{ij}^{new} = e_{ij}^{new} + \left(ke_{ij}^{new} - 1/4 \sum_{\text{nodes of } ij} 1/2(u^2 + v^2)^{new} \right). \quad (15)$$

We note that by linearity steps 6 and 7 are equivalent to remapping total energy using edge internal and kinetic energies to define edge total energies and then computing the internal energy by subtracting the kinetic energy defined by the remapped velocities from the remapped total energy.

The remap algorithm described above is independent of the specific manner in which edge values are computed. We now describe one algorithm for computing these values, the corner transport upwind algorithm due to Colella (1990) as formulated for moving quadrilateral grids by Bell *et al.* (1989). The description applies to both cell-centered and node-centered control volumes. The algorithm has two basic steps. First, left and right (top and bottom) states are determined at each ξ - (η -) edge by a first-order Taylor expansions in space and time. A unique edge value is then determined by upwinding with $-\delta\sigma$ or $-\delta m$. In other words, if $-\delta\sigma$ or $-\delta m$ is positive, the left or bottom state is chosen; otherwise, the right or top state is chosen.

To perform the Taylor expansion we first compute compute van Leer limited (van Leer, 1979) central differences $\Delta_\xi w$, $\Delta_\eta w$ in ξ - and η - directions. In the ξ - direction, these are computed by

$$\begin{aligned} \Delta_\xi w_{ij} &= \min \left(|\Delta^C w|, 2|\Delta^L w|, 2|\Delta^R w| \right) \times \text{sgn} \left(\Delta^C w \right) \\ &\quad \text{if } \Delta^L w \Delta^R w > 0 \\ &= 0, \text{ otherwise,} \end{aligned}$$

where $\Delta^L w = w_i - w_{i-1}$, $\Delta^R w = w_{i+1} - w_i$, and $\Delta^C w = 1/2(w_{i+1} - w_{i-1})$. The states on the left sides of ξ - edges are defined by

$$w_{i+1/2,j,L}^{n+1/2} = \left(w + \frac{\Delta\xi}{2} w_\xi + \frac{\Delta\tau}{2} w_t \right)_{ij}^n.$$

Similar expressions can be obtained for the right sides of ξ - edges and the top and bottom sides of η - edges. Using (12) we can express w_t in terms of spatial derivatives and obtain

$$w_{i+1/2,j,L}^{n+1/2} = \left(w + \left(\frac{\Delta\xi}{2} + \frac{\Delta\tau \mathbf{n}^\xi \cdot \mathbf{s}}{2J} \right) w_\xi + \frac{\Delta\tau \mathbf{n}^\eta \cdot \mathbf{s}}{2J} w_\eta \right)_{ij}^n.$$

We evaluate w_ξ as $\Delta_\xi w / \Delta\xi$ and w_η as $(w_{i,j+1/2}^p - w_{i,j-1/2}^p) / \Delta\eta$. In the latter expression $w_{i,j+1/2}^p$ is determined by performing one-dimensional Taylor expansions in the η direction, i.e.,

$$w_{i,j+1/2,B}^p = \left(w + \left(\frac{\Delta\eta}{2} + \frac{\Delta\tau \mathbf{n}^\eta \cdot \mathbf{s}}{2J} \right) w_\eta \right)_{ij}^p$$

$$w_{i,j+1/2,T}^p = \left(w - \left(\frac{\Delta\eta}{2} - \frac{\Delta\tau \mathbf{n}^\eta \cdot \mathbf{s}}{2J} \right) w_\eta \right)_{i+1,j}^p,$$

and upwinding the resultant top and bottom edge states.

Higher-order Godunov Scheme

In this section we present the higher-order Godunov scheme due to Colella (Colella *et al.*, 1993) for solving the conservative formulation of the Euler equations (1) in two-dimensional rectangular coordinates. Because the method differs from PPM (Colella and Woodward, 1984) in several significant ways, it is presented almost in its entirety.

The overall algorithm is a spatially operator split scheme with Strang splitting (Strang, 1968). We use a uniform computational grid with cell widths Δx , Δy indexed by i, j . The bounding faces of cell i, j are indexed as $i \pm 1/2, j$ and $i, j \pm 1/2$. The flow variables ρ, u, v , and E are all cell-centered. Let $L_x^{\Delta t}$ and $L_y^{\Delta t}$ denote the numerical solution operator for the x -sweep and y -sweeps. The overall method used to advance the numerical solution U^n from time t^n to $t^{n+1} = t^n + \Delta t^n$ is then

$$U^{n+1} = L_x^{\Delta t^n} L_y^{\Delta t^n} U^n \quad (n \text{ even}), \quad U^{n+1} = L_y^{\Delta t^n} L_x^{\Delta t^n} U^n \quad (n \text{ odd}).$$

The stability restriction on the numerical method is a cumulative restriction resulting from an application of the CFL condition in each sweep, i.e.,

$$\Delta t^n = \min(\Delta t_x^n, \Delta t_y^n),$$

where

$$\Delta t_x^n = \sigma \min_{i,j} \frac{\Delta x}{|u_{i,j}^n| + c_{i,j}^n}, \quad \Delta t_y^n = \sigma \min_{i,j} \frac{\Delta y}{|v_{i,j}^n| + c_{i,j}^n},$$

and σ is a positive constant, $\sigma < 1$.

We now describe the x -sweep in the method; the y -sweep is similar. In the x -sweep, we solve

$$\frac{\partial U}{\partial t} + \frac{\partial F(U)}{\partial x} = 0. \tag{16}$$

In order to formulate the x -sweep, we use the results of a characteristic analysis of the following quasilinear, non-conservative form of (16):

$$\frac{\partial q}{\partial t} + A(q) \frac{\partial q}{\partial x} = 0 \tag{17}$$

where $q = (q_1, \dots, q_5)^T = (\rho, u, v, p, \rho e)^T$,

$$A(q) = \begin{pmatrix} u & \rho & 0 & 0 & 0 \\ 0 & u & 0 & 1/\rho & 0 \\ 0 & 0 & u & 0 & 0 \\ 0 & \rho c^2 & 0 & u & 0 \\ 0 & \rho h & 0 & 0 & u \end{pmatrix},$$

and $h = e + p/\rho$ is the specific enthalpy.

A thermodynamically redundant set of primitive variables is used in the quasilinear form so that the numerical fluxes can be computed as simple functions of q requiring no

equation-of-state evaluations (Colella *et al.*, 1993). Only one equation of state evaluation per computational cell per fractional step in the higher-order Godunov scheme is then required.

The characteristic analysis of the quasilinear system follows. The eigenvalues of A are

$$\lambda_1, \dots, \lambda_5 = u - c, \quad u(\times 3), \quad u + c \quad (18)$$

where c is the sound speed. The matrix of right eigenvectors R of A is

$$\begin{aligned} R &= (r_1 \ r_2 \ r_3 \ r_4 \ r_5) \\ &= \begin{pmatrix} 1 & 1 & 0 & 0 & 1 \\ -c/\rho & 0 & 0 & 0 & c/\rho \\ 0 & 0 & 1 & 0 & 0 \\ c^2 & 0 & 0 & 0 & c^2 \\ h & 0 & 0 & 1 & h \end{pmatrix}. \end{aligned} \quad (19)$$

The corresponding matrix of left eigenvectors $L = R^{-1}$ is

$$L = \begin{pmatrix} l_1 \\ l_2 \\ l_3 \\ l_4 \\ l_5 \end{pmatrix} = \begin{pmatrix} 0 & -\rho/(2c) & 0 & 1/(2c^2) & 0 \\ 1 & 0 & 0 & -1/c^2 & 0 \\ 0 & 0 & 1 & 0 & 0 \\ 0 & 0 & 0 & -h/c^2 & 1 \\ 0 & \rho/(2c) & 0 & 1/(2c^2) & 0 \end{pmatrix}. \quad (20)$$

The algorithm to integrate (16) has four general steps. For simplicity, we let U^n and U^{n+1} denote the values of U at the beginning and the end of the x -sweep. The index j is also suppressed. The steps are:

1. Compute monotonicity preserving central difference approximations of Δq in each cell i , where $\Delta q/\Delta x$ is an approximation of $\partial q/\partial x$ at the cell center.
2. Compute time-centered left and right states, $q_{i+1/2,L}^{n+1/2}$ and $q_{i+1/2,R}^{n+1/2}$, at each x -cell face.
3. Solve the Riemann problem at each cell face with the left and right states computed in (2) and evaluate that solution along the ray $x/t = 0$ to obtain $q_{i+1/2}^{n+1/2}$.
4. Compute U_i^{n+1} by conservative differencing.

In step (1), the l -th component of Δq_i , $\Delta q_{i,l}$, is computed using the approach of Colella (1985) (the subscript l is suppressed):

$$\begin{aligned} \Delta_L q_i &= q_i - q_{i-1} \\ \Delta_R q_i &= q_{i+1} - q_i \\ \Delta_C q_i &= 1/2 (q_{i+1} - q_{i-1}) \\ \Delta_{lim} q_i &= \begin{cases} 2 \min(|\Delta_L q_i|, |\Delta_R q_i|), & \text{if } \Delta_L q_i \Delta_R q_i > 0 \\ 0, & \text{otherwise} \end{cases} \\ s &= \begin{cases} 1 & \text{if } \Delta_C q_i > 0 \\ -1 & \text{otherwise} \end{cases} \\ \Delta_f q_i &= s \min(|\Delta_C q_i|, \Delta_{lim} q_i) \\ \Delta q_i &= s \min(|^{4/3} \Delta_C q_i - ^{1/6} (\Delta_f q_{i+1} + \Delta_f q_{i-1})|, \Delta_{lim} q_i). \end{aligned} \quad (21)$$

Slope flattening (Colella, 1989) is used to introduce additional numerical dissipation in the vicinity of shocks. $\Delta q_{i,l}$ is a van Leer limited (van Leer, 1979) fourth-order approximation of $\partial q_l / \partial x$. Fourth-order slopes are not required for accuracy in the scheme. Their use, however, does result in sharper representations of discontinuities (Colella, 1985).

We use Taylor's theorem and equation (17) in the second step to compute left and right states at each cell face. In computing left (right) states, we use a characteristic projection operator (Bell *et al.*, 1989) that discards components in the $\partial q / \partial x$ term corresponding to characteristics which do not originate in the cell to the left (right) of the face. Hence, the left and the right states are computed by

$$\begin{aligned} q_{i+1/2,L}^{n+1/2} &= q_i^n + 1/2 \sum_{k:\lambda_{k,i}>0} \left(1 - \frac{\Delta t}{\Delta x} \lambda_{k,i}\right) (l_{k,i} \cdot \Delta q_i) r_{k,i} \\ q_{i+1/2,R}^{n+1/2} &= q_{i+1}^n - 1/2 \sum_{k:\lambda_{k,i+1}<0} \left(1 + \frac{\Delta t}{\Delta x} \lambda_{k,i+1}\right) (l_{k,i+1} \cdot \Delta q_{i+1}) r_{k,i+1}. \end{aligned}$$

In step (3), we obtain at each x -cell face an approximate solution, $q_{i+1/2}^{n+1/2}$,

$$q_{i+1/2}^{n+1/2} = \left(\rho_{i+1/2}^{n+1/2}, u_{i+1/2}^{n+1/2}, v_{i+1/2}^{n+1/2}, p_{i+1/2}^{n+1/2}, (\rho e)_{i+1/2}^{n+1/2}\right)^T \equiv q_G,$$

to the Riemann problem with left and right states

$$q_L = q_{i+1/2,L}^{n+1/2}, \quad q_R = q_{i+1/2,R}^{n+1/2}. \quad (22)$$

The details of the solution are reviewed below.

The last step uses the Riemann problem solution to conservatively update the value U at the end of the x -sweep:

$$U_i^{n+1} = U_i^n + \frac{\Delta t}{\Delta x} \left(F_{i-1/2}^{n+1/2} - F_{i+1/2}^{n+1/2}\right). \quad (23)$$

$F_{i+1/2}^{n+1/2}$ denotes the evaluation of $F(U)$ using the primitive variables $q_{i+1/2}^{n+1/2}$. In regions of convergent flow, an explicit diffusive flux (Colella and Woodward, 1984) is added to the numerical flux $F_{i+1/2}^{n+1/2}$ in order that a small amount of additional numerical dissipation be present in the vicinity of shocks.

We now review the approximate Riemann solver (Colella *et al.*, 1993) used to solve the Riemann problem for gas dynamics in one space dimension defined by the left and right states given in (22). The solver begins by computing the phase-space solution. The states at the contact discontinuity, p^* , u^* , $\rho_{L/R}^*$, $(\rho e)_{L/R}^*$, $v_{L/R}^*$, are found by applying a variation of Roe's approximate Riemann solver (Roe, 1981) to the quasilinear Lagrangian equations, $\partial q / \partial t + B(q) \partial q / \partial m = 0$, where $q = (\rho, u, v, p, \rho e)^T$, m is the mass coordinate,

$$B(q) = \begin{pmatrix} 0 & \rho^2 & 0 & 0 & 0 \\ 0 & 0 & 0 & 1 & 0 \\ 0 & 0 & 0 & 0 & 0 \\ 0 & C^2 & 0 & 0 & 0 \\ 0 & h\rho^2 & 0 & 0 & 0 \end{pmatrix},$$

and $C = \rho c$. The eigenvalues of B are $\lambda_1, \dots, \lambda_5 = -C, 0(\times 3), C$. We evaluate the right eigenvectors of A associated with the eigenvalues of $-C$ and C at q_L and q_R , respectively:

$$\begin{aligned} r_- &= (r_{-,1}, \dots, r_{-,6}) = (-\rho_L^2, C_L, 0, 0, -C_L^2, -h_L \rho_L^2)^T \\ r_+ &= (r_{+,1}, \dots, r_{+,6}) = (-\rho_R^2, -C_R, 0, 0, -C_R^2, -h_R \rho_R^2)^T. \end{aligned}$$

The three eigenvectors for the eigenvalue 0 do not contribute to the jumps in u and p . Hence, the jumps in q can be expressed by

$$\begin{aligned} u_R - u_L &= \alpha_- r_{-,2} + \alpha_+ r_{+,2} = \alpha_- C_L - \alpha_+ C_R \\ p_R - p_L &= \alpha_- r_{-,5} + \alpha_+ r_{+,5} = -\alpha_- C_L^2 - \alpha_+ C_R^2 \\ q_{L/R,i}^* &= q_{L/R,i} \pm \alpha_{\mp} r_{\mp,i} \quad \text{for } q_i = \rho, v, \rho e \end{aligned}$$

Solving for α_{\pm} , we obtain

$$\begin{aligned} u^* &= (u_L C_L + u_R C_R + p_L - p_R) / (C_R + C_L) \\ p^* &= (p_L C_R + p_R C_L + (u_L - u_R) C_R C_L) / (C_R + C_L) \\ \rho_{L/R}^* &= \rho_{L/R} + (p^* - p_{L/R}) / c_{L/R}^2 \\ (\rho e)_{L/R}^* &= (\rho e)_{L/R} + (p^* - p_{L/R}) h_{L/R} / c_{L/R}^2 \\ v_{L/R}^* &= v_{L/R}. \end{aligned}$$

The second step is to evaluate the physical space solution along the ray $x/t = 0$ to obtain q_G . We first define

$$\begin{aligned} q, q^* &= \begin{cases} q_L, q_L^* & \text{if } u^* > 0 \\ q_R, q_R^* & \text{otherwise} \end{cases} \\ \Gamma^* &= \begin{cases} c_L^2 \rho_L / p_L & \text{if } u^* > 0 \\ c_R^2 \rho_R / p_R & \text{otherwise} \end{cases} \\ (c^*)^2 &= \Gamma^* p^* / \rho^* \\ \lambda, \lambda^* &= \begin{cases} u_L - c_L, u^* - c^* & \text{if } u^* > 0 \\ u_R + c_R, u^* + c^* & \text{otherwise} \end{cases} \\ s &= \begin{cases} -1 & \text{if } u^* > 0 \\ 1 & \text{otherwise.} \end{cases} \end{aligned}$$

If $p^* > p$, then the wave separating q and q^* is a shock. We compute an approximate Lagrangian shock speed by $W = (\rho c + \rho^* c^*) / 2$. The approximate Eulerian shock speed is then $\sigma = u^* + sW / \rho^*$. We then set

$$q_G = \begin{cases} q & \text{if } s\sigma < 0 \\ q^* & \text{otherwise.} \end{cases}$$

The wave separating q and q^* is otherwise a rarefaction. We first enforce $s\lambda \geq s\lambda^*$ by flooring $s\lambda$ as follows: $\lambda = s \max(s\lambda, s\lambda^*)$. We then set

$$q_G = \begin{cases} q & \text{if } s\lambda \leq 0 \\ q^* & \text{if } s\lambda^* \geq 0 \\ \frac{\lambda q^* - \lambda^* q}{\lambda - \lambda^*} & \text{otherwise;} \end{cases}$$

the last expression uses linear interpolation in the characteristic speed to approximate the solution inside the rarefaction.

Numerical results

In this section we compare the accuracy and performance of the two methods described above for a series of test problems. We also examine the effect of changing some of the algorithmic options and parameters in the Lagrange plus remap scheme. For the Lagrange step, we compare a number of time centering options: the use of the midpoint method as the predictor-corrector, the use of an updated q in the corrector, and the forgoing of the prediction of U in the predictor. We also examine the use of the standard Lagrange viscosity instead of the monotonic q and the effect of the hourglass filter. For the remap step, we compare the use of a spatially operator split advection algorithm instead of the corner transport upwind scheme. We also look at the effect of using different limiters and consider advecting E directly instead of e and ke . We also explore the effects of relaxing numerical conservation of E , in particular, using (15) only in the vicinity of a shock or only if (15) increases e .

For all problems, we use a uniform grid of square cells. The CFL number is .9 unless noted otherwise. For the Lagrange plus remap scheme we have chosen to disable the hourglass filter by default.

Interacting blast wave. The flow domain for this one-dimensional problem (Woodward and Colella, 1984; Christensen, 1990) has length one with reflecting walls at both end. The gas is polytropic with $\gamma = 1.4$. At $t = 0$ the gas is at rest with density 1. The initial pressure is 1000 in the leftmost tenth of the domain, 100 in the rightmost tenth, and .01 elsewhere. Initially, two shock waves and two contact discontinuities develop at the initial discontinuities and propagate towards one another, while two rarefactions develop, propagate towards the walls, and reflect off them. As time progresses, these six initial waves interact and create additional contact discontinuities.

Figure 4 displays the density computed by the higher-order Godunov and the Lagrange plus remap schemes at $t = .038$ on a 1200 zone domain. To obtain a baseline solution, we also compute the flow both with a Lagrangian higher-order Godunov method (Saltzman and Colella, 1985) and with the staggered grid Lagrange scheme on 3600 zone domains. The initial zoning for both Lagrangian computations is spatially uniform. The densities at $t = .038$ for all four computations are displayed in Figure 4. The two Lagrangian solutions are virtually indistinguishable and therefore serve as a baseline solution. We note that these solutions themselves have a flaw, a spurious overshoot at $x \approx .765$. The magnitude of the overshoot is the only discernible difference between the two sets of Lagrangian results. This overshoot has been previously observed (Christensen, 1990).

From Figure 4 we see that the higher-order Godunov scheme better matches the density peak at $x \approx .75$, while the Lagrange plus remap scheme shows a slight overshoot here. On the other hand the latter shows sharper resolution of the contact discontinuities at $x \approx .6$ and $x \approx .75$. The density between $x \approx .65$ and $x \approx .75$ also seems to be better represented by the Lagrange plus remap scheme. We note that the PPM results in (Woodward and Colella, 1984) show much better resolution of the contact discontinuities than the Godunov scheme used here. The implementation of PPM used for those results includes a contact detection

and steepening scheme. If that scheme is disabled, the PPM results are essentially the same as those obtained here (Colella, 2000). Contact detection and steepening is not implemented in the present scheme because parabolic interpolation appears to be essential to its success. Moreover, steepening appears to introduce spurious numerical artifacts in multidimensional calculations.

We next examine the effect of advecting E directly as opposed to advecting e and ke separately. Note that when E is advected directly, the remapped value of e is defined as the difference between E and the kinetic energy found from the remapped velocity. In the upper plot of Figure 5 we see the results at $t = .038$ for three Lagrange plus remap calculations. The first density profile shows the same results displayed in Figure 4. The second profile plots the density when E is advected directly. This profile contains a number of noticeable deficiencies. Woodward and Colella (1984) observed that these deficiencies were due to the computation of unphysically high densities at early time. They corrected the problem by using a minmod limiter in the advection step. The third profile shows our results for this strategy. Note that these results are similar to those found with BBC by Woodward and Colella (1984).

In the lower half of Figure 5, we examine the early time behavior of the two energy remap approaches employing van Leer limiters. We indeed see that when E is advected directly, the density at early time is much higher than when e and ke are remapped separately. Moreover, we see that the problem actually worsens as the CFL number is lowered. We conjecture that when e and ke are remapped separately, the early time overshoots are reduced because the effective total energy slopes are limited to a slightly greater amount.

We also consider the effects of different strategies for energy conservation. In Figure 6 we see the results at $t = .038$ for four Lagrange plus remap calculations, each using a different strategy. The first strategy is to always conserve E . This is our default strategy, so the results here are identical to those in Figure 4. The second strategy is to conserve E only at shocks. This strategy is implemented by using equation (15) only if q exceeds some threshold. The third strategy is to conserve E only at shocks and only if using (15) increases the internal energy (Benson, 1992). The last strategy is to conserve E regardless of the presence of shocks but only if using (15) increases the internal energy. We see very little difference between the first and the second strategies. With the latter two we see large errors in the solution, including incorrect shock and contact discontinuity locations.

Double Mach reflection of a strong shock. For this problem (Woodward and Colella, 1984) we use a flow domain of length 3.5 and width 1.0. At $t = 0$ a Mach 10 planar shock in a $\gamma = 1.4$ polytropic gas impinges at an angle of 60° on the lower face of the domain at a distance of .3 from the left end of the domain. The preshock density and pressure are 1.4 and 1, respectively. The lower face of the domain is treated as a reflecting wall to the right of the impingement point; to the left, it is treated as an outflow boundary. (The initial shock position and the treatment of the lower boundary, which do differ slightly from those used by Woodward and Colella (1984), were used previously by Pember *et al.* (1995).) At the top face we impose inflow boundary conditions matching the exact evolution of the shock as it traverses the boundary. The other boundary conditions are inflow at the left and outflow at the right. The flow is self-similar and characterized as follows. The first reflected shock, the incident shock, and the first Mach stem meet at a triple point. The first contact

interacting blast wave: rho at t = 0.03800

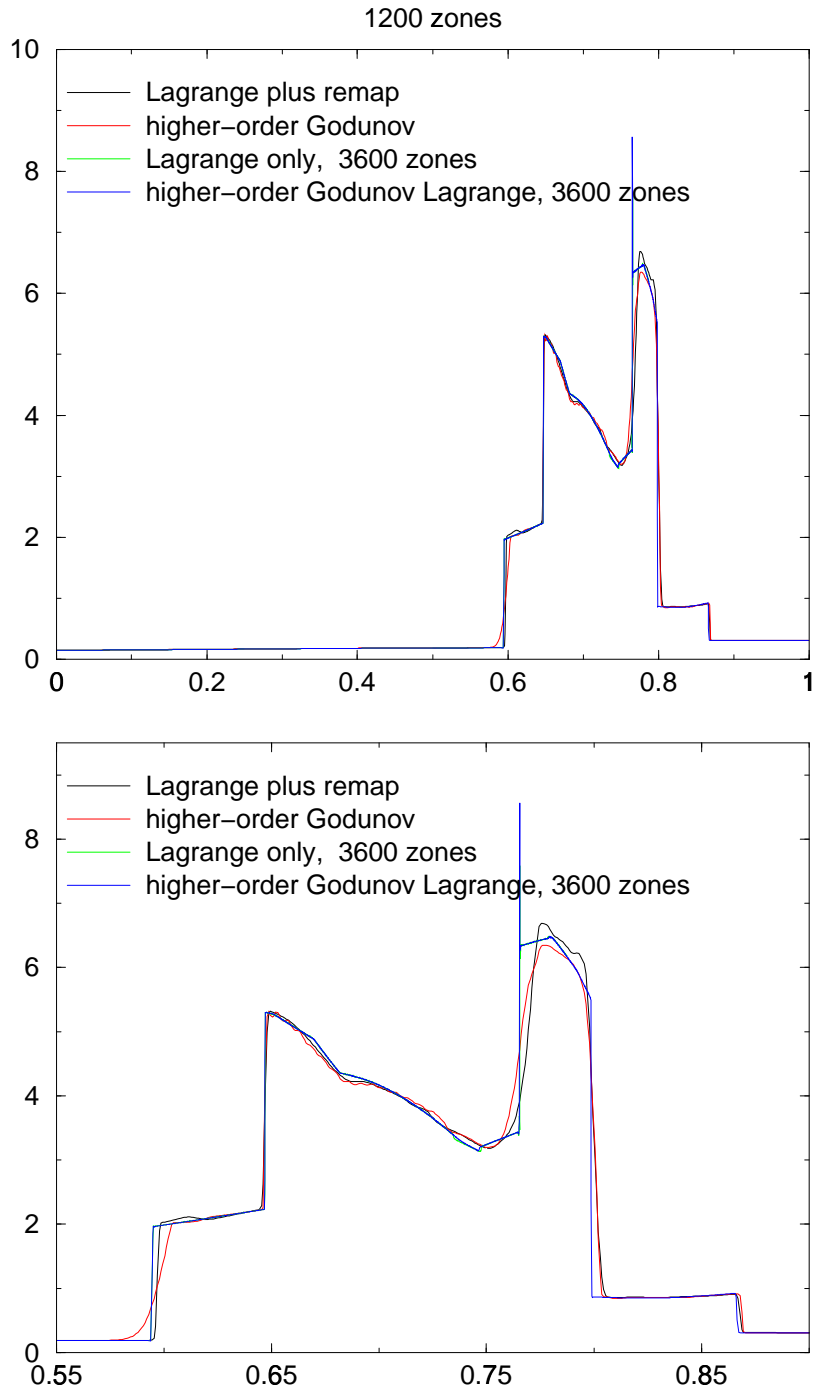


Figure 4: Computed density at $t = .038$ for the interacting blast wave problem. The upper and lower plots show the whole domain and a closeup, respectively.

interacting blast wave: rho at t = 0.03800

1200 zones total on [0,1]

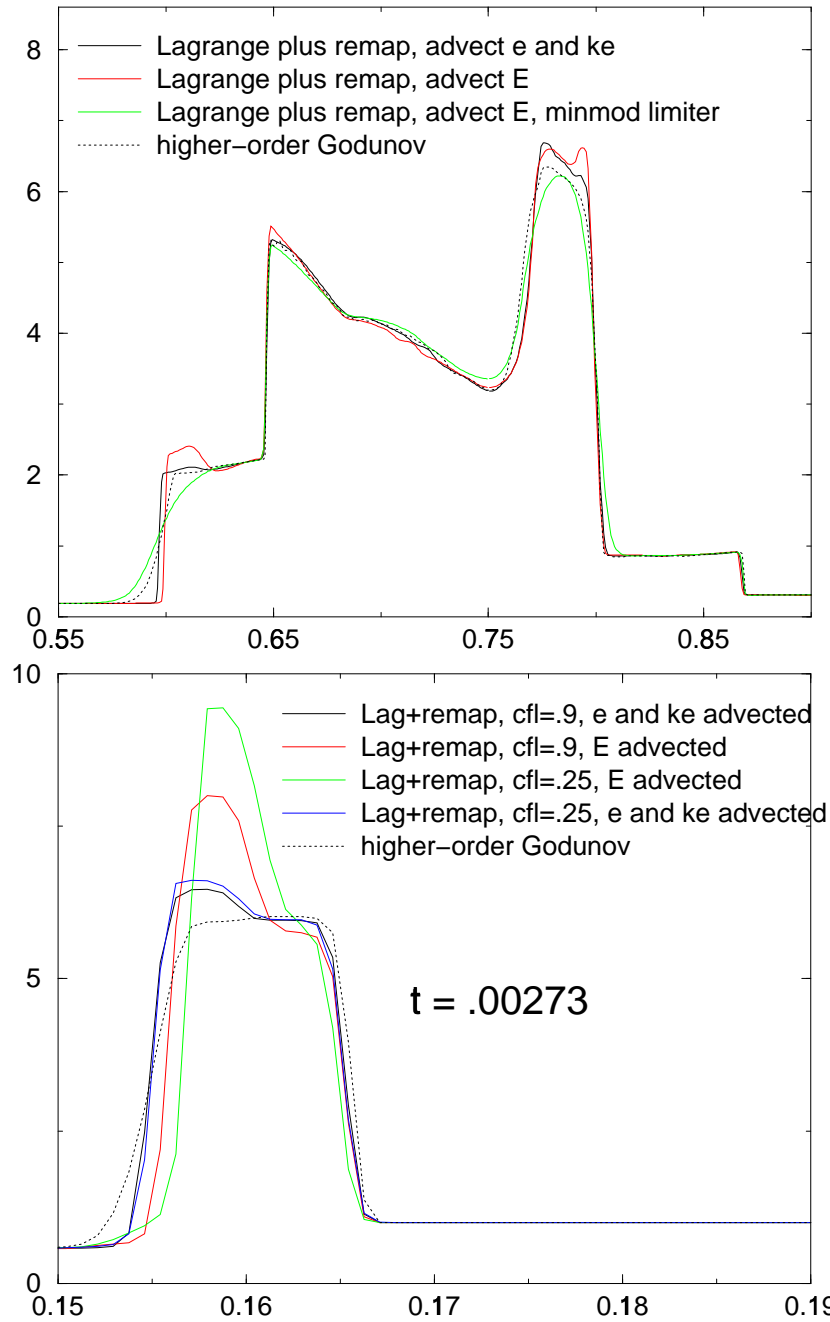


Figure 5: The upper plot shows a closeup of the computed density at $t = .038$ for the interacting blast wave problem obtained by the Lagrange plus remap scheme with three variations of energy advection. The lower plot shows a closeup of the density at $t = .00273$ for two of these. Higher-order Godunov results are shown in both plots for comparison.

interacting blast wave: rho at t = 0.03800

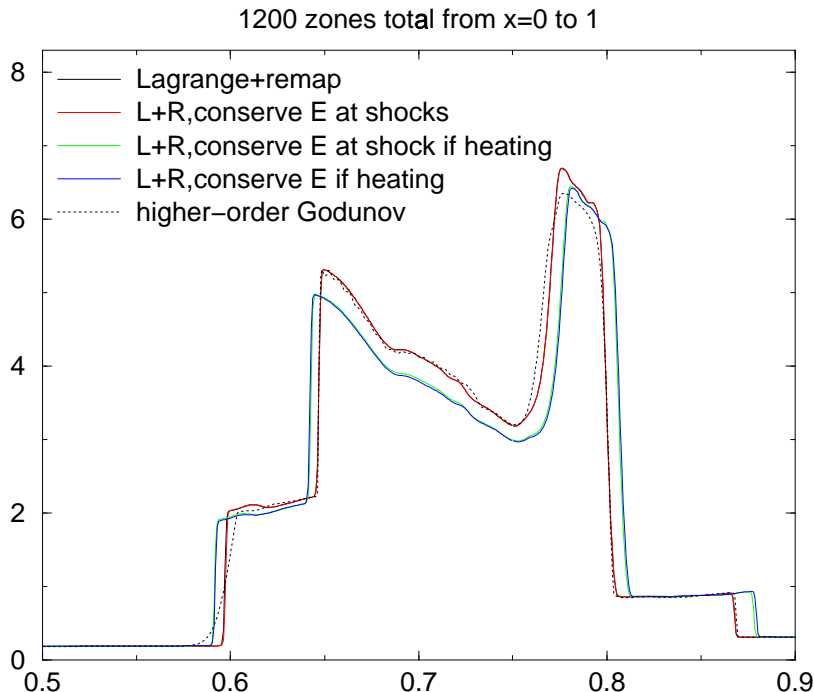


Figure 6: Four different strategies for energy conservation are compared. Higher-order Godunov results are shown for comparison.

discontinuity extends from this triple point down to the reflecting wall, at which point it is deflected into a wall jet that flows back towards the Mach stem. The contact discontinuity and wall jet exhibit small rollups induced by a Kelvin-Helmholtz instability. The wall jet also displays a larger rollup induced by the presence of the Mach stem. A curved reflected shock is connected to the first reflected shock. A second weaker Mach stem extends from this point to the first contact discontinuity. There is also a second slipline attached to this point which is too weak to appear in our computational results.

We compute the flow on a 1120×320 grid with the two methods. The density at $t = .21$ is displayed in Figure 7. The higher-order Godunov scheme is slightly better at both suppressing oscillations in the postshock region of the left end of the curved reflected shock and not suppressing the small rollups in the wall jet. The results also show a slightly smaller rollup of the wall jet just before the Mach stem. The Lagrange plus remap scheme, on the other, is better at suppressing oscillations in the middle and right sections of the postshock region of the curved reflected shock. Both schemes exhibit a spurious wave emanating where the Mach 10 shock intersects the top boundary. This wave, also observed by Woodward and Colella (1984) is due to the mismatch between the exact and the numerical representations of the shock outside and inside, respectively, the top boundary. The spurious wave has a slightly more deleterious effect on the Lagrange plus remap solution. The spurious contour in the higher-order Godunov results just outside the curved reflected shock at $x \approx 1.5$, $y \approx .5$ delimits a small perturbation that is also present in the Lagrange plus remap results but which does not appear in the plot with our choice of contour levels.

We next explore the effect of three different timestepping options in the Lagrange plus

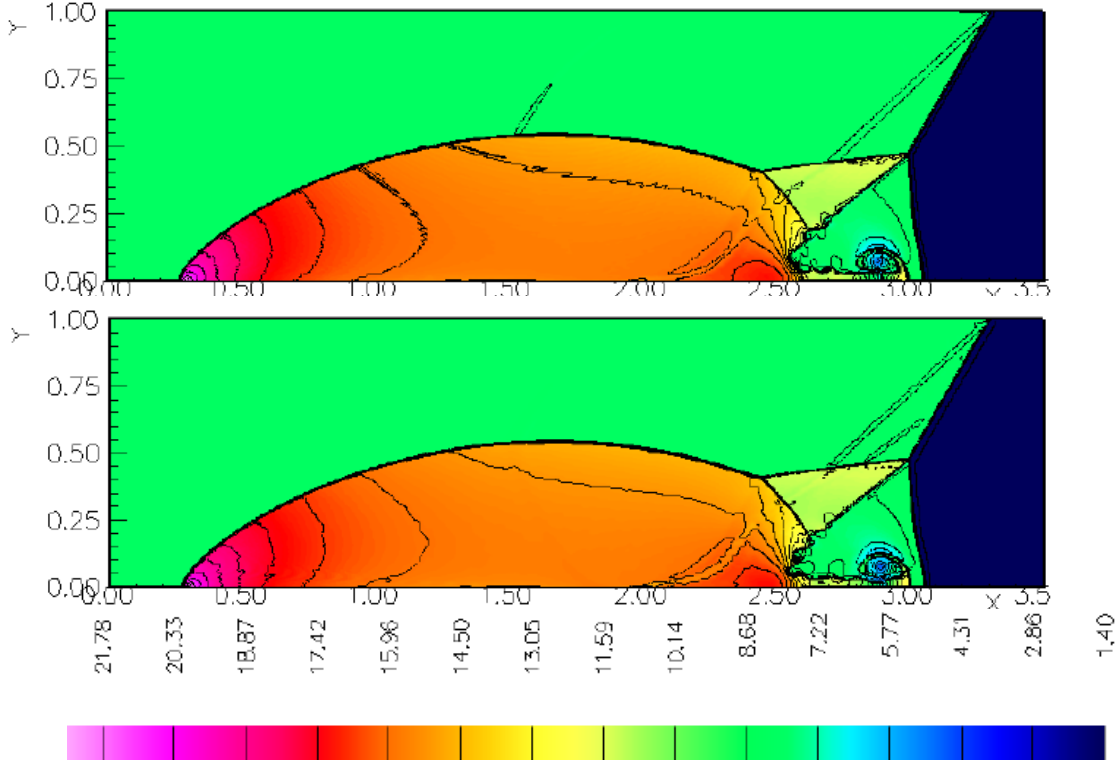


Figure 7: Density contours from calculations of a Mach 10 shock propagating in a polytropic gas ($\gamma = 1.4$) at 30° to the vertical impinging on a solid wall. Thirty density contours are used in each plot. The density contours range from 1.4 to 22.51. The upper plot is computed with the higher-order Godunov scheme, the lower with the Lagrange plus remap scheme.

remap scheme on the solution. The first option is to recompute q in the corrector, the second is to forgo velocity prediction in the predictor, and the third is to use the midpoint method as the predictor-corrector scheme. The density at $t = .21$ computed with each of these options is displayed in Figure 8. For the first two options the solutions show no significant differences with the results in Figure 7. With the midpoint method, however, there are somewhat fewer oscillations in the density field in the postshock region of the reflected shock.

The effect of the hourglass filter in the Lagrange step on the solution is examined next. Margolin and Pyun (1987) define α to be one fourth the ratio of the computational time step to the time needed for the hourglass filter to fully effect the solution. The maximum stable value of α is .25 because in two dimensions each vertex is shared by four cells. They found, however, values of α between .01 and .05 to be sufficient for most problems. The densities at $t = .21$ for $\alpha = .01$, .05, and .25 are displayed in Figure 9. The maximum value of α completely suppresses the small rollups in the wall jet, while those rollups are only moderately suppressed with the other two values. The results again otherwise do not differ significantly from those in Figure 7; note that those results correspond to $\alpha = 0$.

We note that that the Kelvin-Helmholtz instability in question is observed neither in the computational results of Woodward and Colella (1984) nor in the experimental data reported by Glaz *et al.* (1985). In the case of the numerical results, the issue was simply one of resolution. The instability is observed in more highly resolved calculations; see, for

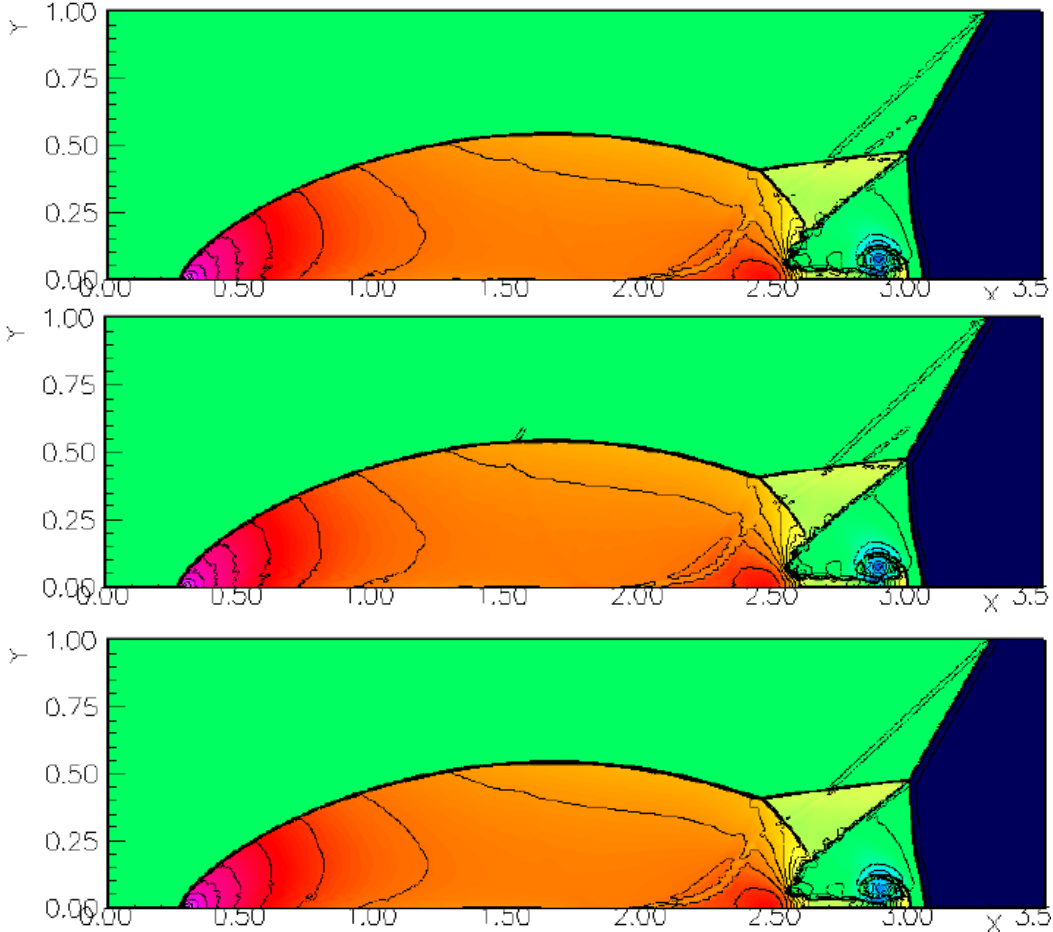


Figure 8: Density contours computed by the Lagrange plus remap scheme with three different timestepping options: recomputing q in the corrector step (upper plot), forgoing velocity prediction in the predictor (middle), and using the midpoint method as the predictor-corrector (lower). The contour scale is the same as in Figure 7.

example, Berger and Colella (1989). The experimental data do not show any small rollups because the physical viscosity is sufficiently large to suppress them (Colella, 2000). The physical viscosity is large, in turn, because low pressures (.1 atm or less) and densities are necessary to generate strong shocks in the laboratory. Higher kinematic viscosities, and therefore greater dissipation, result.

We also examine the effect of using a spatially operator split advection scheme. We consider two different formulations. The first uses $\xi\eta\eta\xi$ and $\eta\xi\xi\eta$ sweep patterns in alternate timesteps, each sweep taking half a pseudo-timestep. The other alternates $\xi\eta$ and $\eta\xi$ sweep patterns, each sweep taking a full pseudo-timestep. The densities at $t = .21$ computed with the two approaches are displayed in Figure 10. We again see that the instabilities along the wall jet are suppressed, although less so with the second approach. The results otherwise do not differ significantly from those in Figure 7.

We next examine the effect of using the standard Lagrange viscosity. The computed density at $t = .21$ is shown in Figure 11. Using the standard Lagrange viscosity results

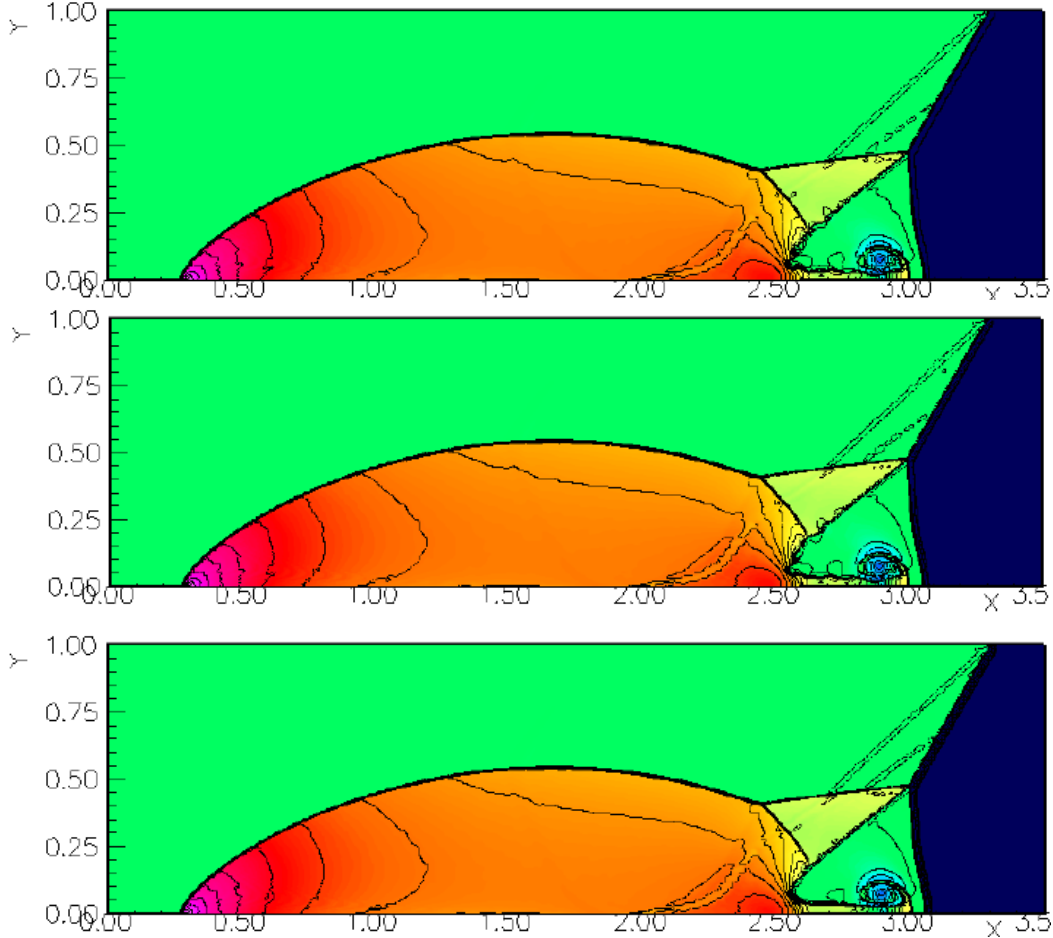


Figure 9: Density contours computed by the Lagrange plus remap scheme with three different values of the hourglass filter parameter α . The results for $\alpha = .01$, $.05$, and $.25$ are shown in the top, middle, and bottom plots, respectively. The contour scale is the same as in figure 7.

in a poor representation of the Mach stem extending down from the kink in the reflected shock. This poor representation is also present in the BBC results reported by Woodward and Colella (1984) where it is attributed to the linear viscosity term. Otherwise, the results are again otherwise essentially the same as those in Figure 7.

We finally report some timing results for this problem as run serially on a single processor on the LLNL Tera cluster, i.e., a single 533 MHz Compaq Alpha processor. The timings are reported for the integration portion of the codes only; we do not include time to perform output, etc. We report serial rather than parallel timings because the purpose here is to compare the efficiency of the underlying algorithms, not their implementations on parallel architectures. For the Lagrange plus remap run, we used the midpoint rather than the Heun method for the predictor. However, we made no optimizations to account for the fact that the grid was comprised of square and not general quadrilaterals. The Lagrange plus remap scheme took 1591 time steps and 17061 seconds to compute to $t = .21$. The Lagrange and remap steps took 4830 and 12330 seconds, respectively. The corresponding times per zone per time step were $8.47 \mu\text{sec}$ and $21.45 \mu\text{sec}$. The higher order Godunov run took 1916 time

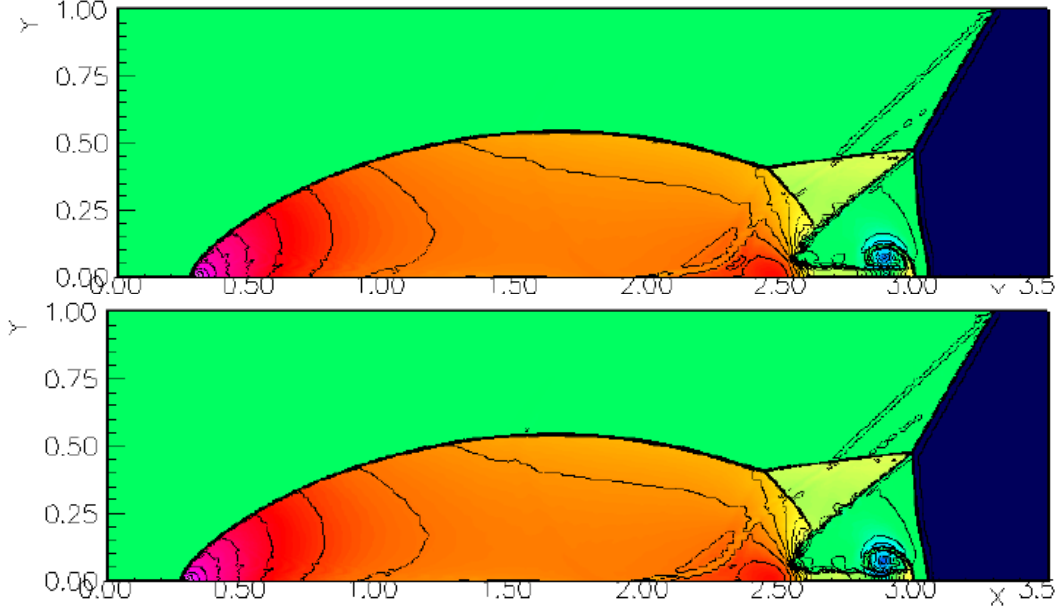


Figure 10: Density contours for double Mach reflection problem computed by the Lagrange plus remap scheme with two spatially operator split advection schemes. The results on top correspond to alternating $\xi\eta\eta\xi$ and $\eta\xi\xi\eta$ sweep patterns, those on the bottom to $\xi\eta$ and $\eta\xi$ patterns. The contour scale is the same as in Figure 7.

steps and 12110 seconds to compute to the final time. The time per zone per time step was $17.63 \mu\text{sec}$. Woodward and Colella reported BBC run times that showed the scheme to be approximately 4 times faster than PPM. We note, however, that these were reported for one space dimension only. Moreover, the higher-order Godunov scheme used here is faster than PPM by virtue of its use of linear rather than parabolic profiles and its lack of contact steepening. Finally, the Lagrange plus remap run times are comparable to run times we have seen for implementations of spatially unsplit higher-order Godunov schemes.

Cylindrical Sedov problem. The initial conditions for the cylindrical Sedov problem (Sedov, 1959) consist of a no flow, uniform density field. The energy is zero everywhere except at the origin. The flow is self-similar and consists of a cylindrically symmetric wave, the leading edge of which is a shock of infinite strength. We use a unit square flow domain to compute the solution on one quadrant. The blast location is at the origin. The blast energy is 8, $\gamma = 5/3$, and initially $\rho = 1$. A specific internal energy of $2/\Delta x^2$ is specified in the cell adjacent to origin because we compute only one quadrant of the solution.

We compute the solution on 50×50 and 200×200 grids with both methods. The computed and exact solutions at $t = .1$ along the rays $x = 0$ and $x = y$ are displayed in Figure 12. On the 50×50 grid, the Godunov solution along $x = y$ better matches the exact solution until $r \approx .575$ beyond which the Lagrange plus remap solution was the better match. Along $x = 0$, both solutions are comparable. On the 200×200 grid there is little difference between the methods except near the shock. On both grids the Lagrange plus remap solution better matches the peak density at the shock front.

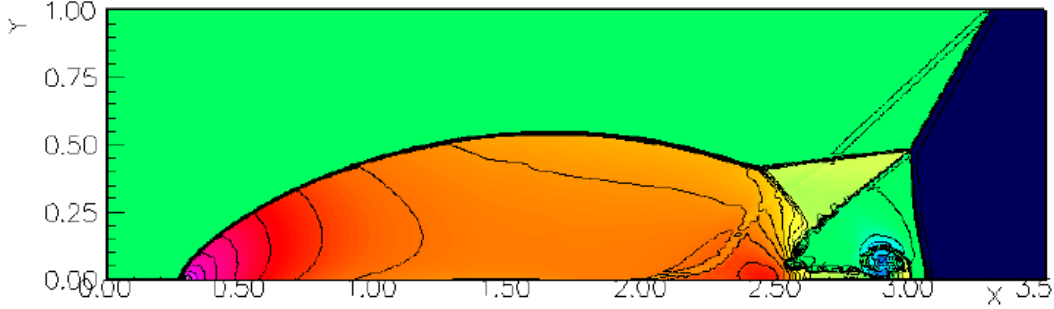


Figure 11: Density contours computed by the Lagrange plus remap scheme using the standard Lagrange viscosity. The contour scale is the same as in Figure 7.

Refraction of an oblique shock wave at a density interface. In this problem we model a shock ($M \approx 1.89$) in a $\gamma = 1.4$ polytropic gas impinging on a density interface at an angle of incidence of 58° . The preshock conditions in cgs units are $u = v = 0$ and $p = 1.01325 \times 10^6$. The preshock densities are 1.223×10^{-3} upstream of the interface and 6.243×10^{-3} downstream. The postshock conditions are $u = 3.862384 \times 10^4$, $v = 0$, $\rho = 3.0578669 \times 10^{-3}$ and $p = 4.0502098 \times 10^6$. The flow domain is 1.12 cm wide by .72 cm high. The initial shock location is .2 cm from the left boundary and the density interface intersects the lower boundary .0975 cm further to the right. Reflecting wall boundary conditions are imposed at the upper and lower faces. The other boundary conditions are inflow at the left and outflow at the right.

This problem is a simplification of one in which a Mach 1.89 shock refracts at an air/SF₆ interface (Henderson and Puckett, 1993), the simplification being the treatment of both gases as polytropic with equal γ 's of 1.4. This refraction is categorized as a Mach-reflection-refraction (MRR) in the strong incident shock group at a fast-slow gas interface (Abd-El-Fattah and Henderson, 1978). Even with our simplifying assumptions the flow is still in this regime. The fast-slow designation implies that the sound speed upstream of the interface is greater than that downstream. Such refractions are characterized as follows. The incident shock, a Mach stem, a curved reflecting shock, and a weak contact discontinuity (not visible in our results) meet at a triple point. The contact extends from the triple point to the deflected density interface. Upstream of this intersection, the deflected density interface is characterized by rollups induced by a Kelvin-Helmholtz instability. A transmitted shock propagates into the denser fluid. The presence of the lower wall induces two additional flow features: the density interface undergoes rollup and the transmitted shock undergoes direct Mach reflection.

We compute the flow on a 896×576 grid with the two methods. The density at $t = 1.16667 \times 10^{-5}$ seconds is displayed in Figure 13. The results mainly differ along the density interface and near the triple point. The Lagrange plus remap code computes a slightly more irregular rollup pattern and a slightly faster growth rate of the shear layer than does the higher-order Godunov code. The Lagrange plus remap algorithm computes a Mach stem height of .028 cm and an angle between the reflected shock and the Mach stem of 70° . The higher-order Godunov algorithm computes corresponding values of .019 cm and 60° . Both codes, however, compute the same location of the Mach stem and the same angle between the Mach stem and the interface, namely, 78° .

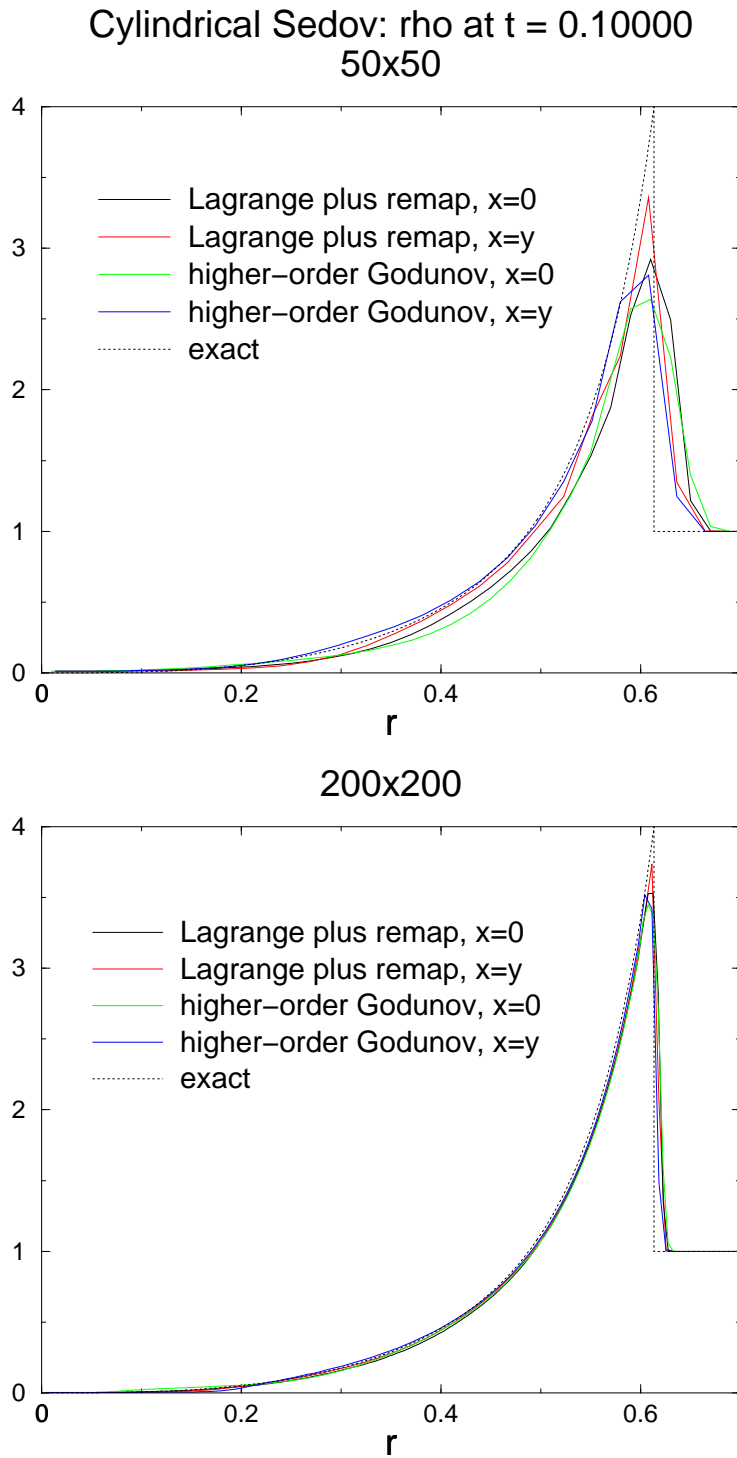


Figure 12: Computed solutions to the cylindrical Sedov problem.

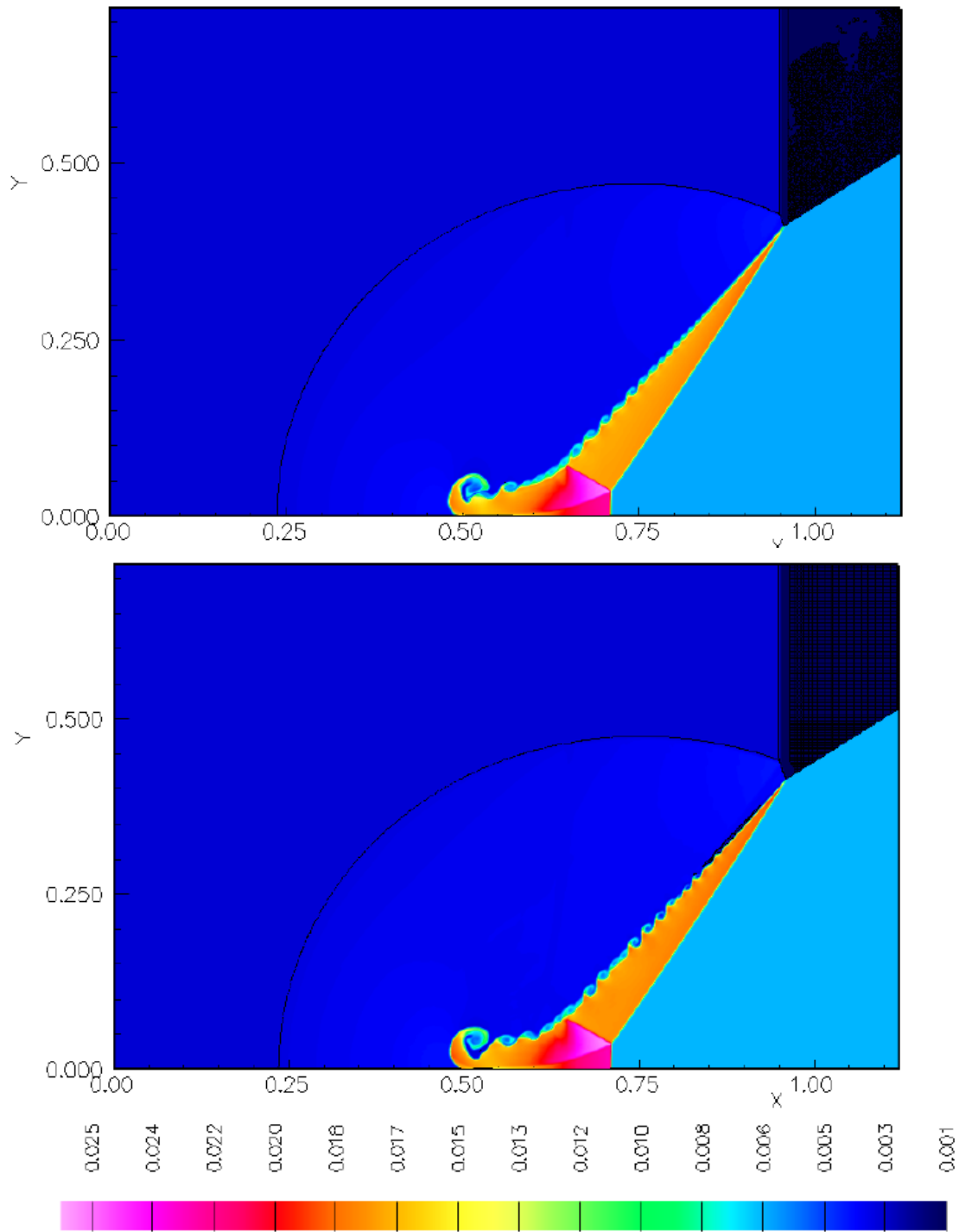


Figure 13: Density from calculations of a Mach 1.89 shock in a $\gamma = 1.4$ polytropic gas impinging on a density interface at an angle of 58° . The density ranges from .001223 to .026083. A single contour level shows the position of the curved reflected shock. The upper plot is computed with the higher-order Godunov scheme, the lower with the Lagrange plus remap scheme.

We next look at the effect of both the CFL number σ and the use of the hourglass filter. The upper two plots in Figure 8 show results for both schemes with $\sigma = .25$. In both cases the shock and the discontinuity locations are the same as in the $\sigma = .9$ results, but the rollups along the density interface are suppressed. The lower two plots show results for the Lagrange plus remap scheme with the hourglass filter ($\alpha = .25$) for $\sigma = .9$ and $\sigma = .25$. We see that the hourglass filter itself only slightly suppresses the rollups. When $\sigma = .25$, the rollups are almost entirely suppressed but to no greater extent than with the higher-order Godunov scheme at the same value of σ .

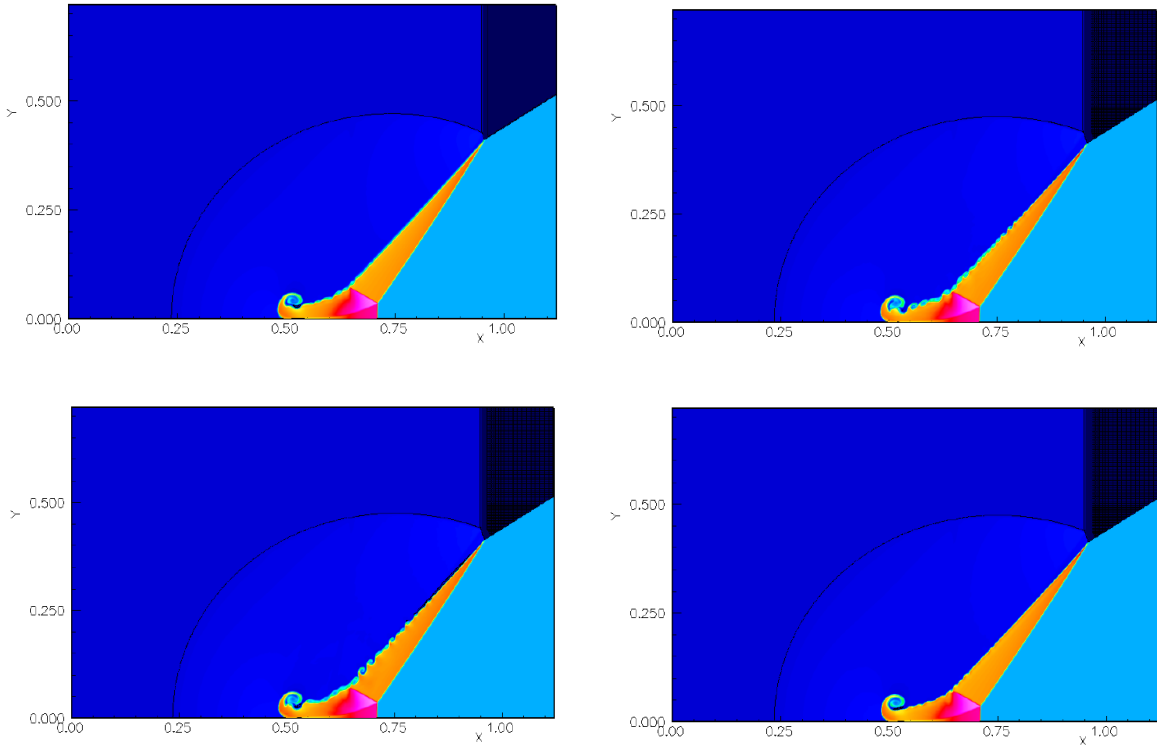


Figure 14: Density for the shock refraction problem. From left to right and then top to bottom the results were computed with the higher-order Godunov scheme with $\sigma = .25$, and the Lagrange plus remap scheme with $\sigma = .25$, with the hourglass filter on and $\sigma = .9$, and with the hourglass filter on and $\sigma = .25$. The scale is the same as in Figure 13.

We finally examine the effect of two integrator options on the solution. The first option is to use the spatially operator split advection scheme that alternates $\xi\eta\eta\xi$ and $\eta\xi\xi\eta$ sweep patterns; the other is to enforce energy conservation only at shocks and only if using (15) increases e . The results are displayed in Figures 15 and 16. In contrast to the results for the blast wave and the Mach reflection problems, we see here no major differences with the results for the standard set of options in Figure 13.

Planar Noh problem. In this one-dimensional problem (Noh, 1987) a $\gamma = 5/3$ polytropic gas has the initial state $(\rho, u, e) \equiv (1, 1, 0)$. At the left and right faces inflow and reflecting wall boundary conditions are imposed. The solution is a shock of infinite strength moving with velocity $-1/3$.

We first compute the flow on a domain of unit length on a grid of 800 zones with the

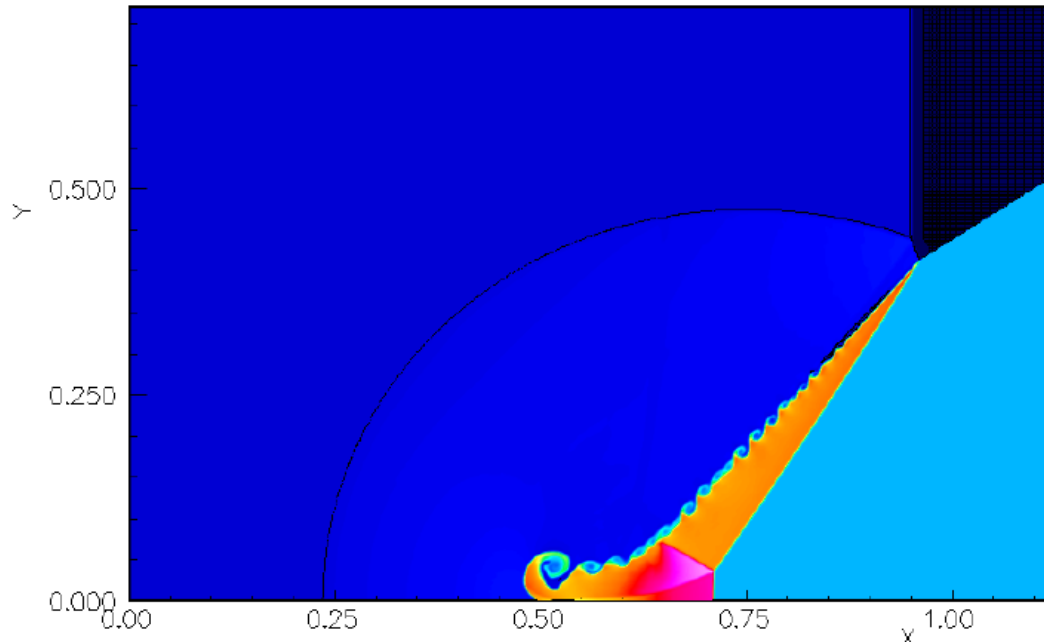


Figure 15: Density contours for the shock refraction problem computed by the Lagrange plus remap scheme with the option to conserve energy only at shocks and only if using (15) increases e . The scale is the same as in Figure 13.

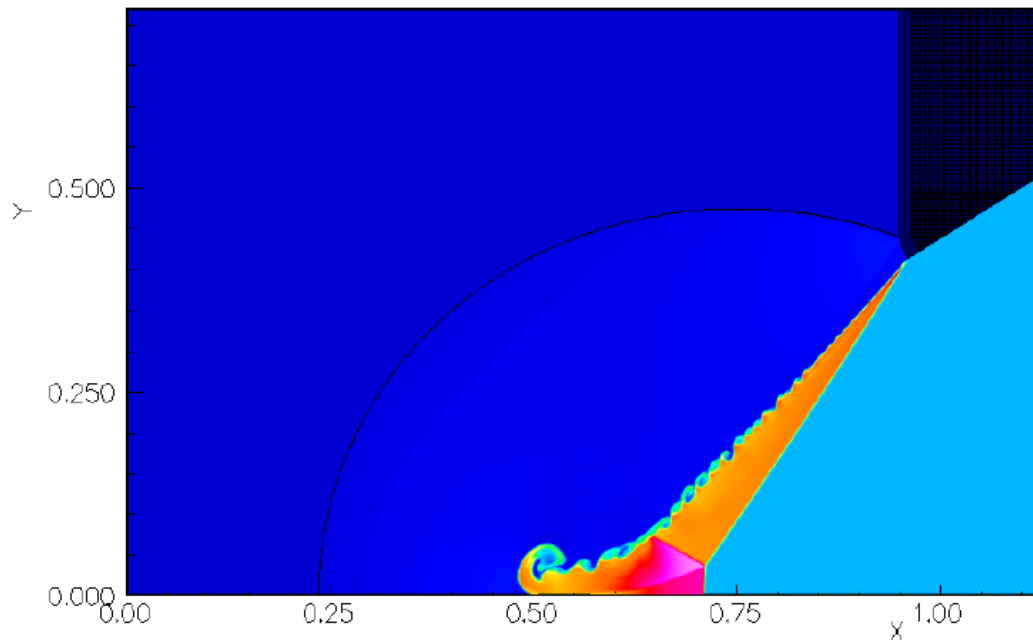


Figure 16: Density contours for shock refraction problem computed by the Lagrange plus remap scheme with a spatially operator split advection scheme. The scale is the same as in Figure 13.

higher-order Godunov method; see Figures 17 and 18. Without modification, the method computes the wrong shock speed. There are essentially three modifications one can make to the method so that it does compute the correct speed: impose the postshock pressure of $\frac{4}{3}$ at the rightmost cell face, use twice the normal Lapidus viscosity at the right most cell face (Greenough, 2000), or use an exact Riemann solver for a polytropic gas instead of the approximate solver; again, see Figures 17 and 18. (The exact solver is exact to the tolerance of the root finder it employs.) The location of the shock in the exact solution at this time is $x = .7567$. All three of these approaches exhibit postshock oscillations. In an attempt to reduce these, we tried a CFL number $\sigma = .5$ with three approaches: the Lapidus viscosity boundary modification, the exact Riemann solver, and the exact Riemann solver with the Lapidus viscosity completely disabled. The last of these shows the least amount of oscillation in in the postshock region, while the first actually shows more oscillations than the $\sigma = .9$ case.

We next compute the flow with the Lagrange plus remap scheme using both the monotonic and the standard artificial viscosity; see Figures 19 and 20. For comparison, we include the higher-order Godunov scheme results computed using the viscosity modification and using the exact Riemann solver with $\sigma = .9$, and using the exact Riemann solver with the Lapidus viscosity completely disabled with $\sigma = .5$. In the wall region, the Lagrange plus remap scheme with the monotonic q and the higher-order Godunov scheme with the viscosity modification compute the least amount of wall heating. Not surprisingly, the use of the standard q results in the largest amount of wall heating. In the postshock region, the standard q and the $\sigma = .5$ results show the least amount of oscillation. The higher-order Godunov scheme with the viscosity modification computes the most, while the other two schemes are comparable. The solution computed by two exact Riemann solver methods show the best resolution of the shock. The Lagrange plus remap results show slightly more spreading of the shock, while the shock speed in the approximate Riemann solver results is slightly underestimated.

LeBlanc shock tube. In this shock tube problem (Benson, 1992a; LeBlanc) the initial discontinuity separates a region of very high energy and density from one of low energy and density. The initial discontinuity is at $x = 3$. $(\rho, e, u) = (1, .1, 0)$ for $x < 3$ and $(.001, 10^{-7}, 0)$ for $x > 3$. The gas is polytropic with $\gamma = 5/3$. The solution consists of a strong rarefaction moving to the left, and a contact discontinuity and a shock moving to the right.

We compute the flow with both methods on grids of 180 and 1440 zones. For comparison, we also compute the flow both with a Lagrangian higher-order Godunov method (Saltzman and Colella, 1985) and with the staggered grid Lagrange scheme on the same domain. We also compute the exact solution using the exact Riemann solver mentioned above. The internal energies for all four methods and both grids as well the exact solution at $t = 6$ are shown in Figures 21 and 22. On the 180 zone grid, all four methods have difficulty computing the position of the shock. The two Lagrangian methods best compute this position, while the two Eulerian scheme show roughly equal and opposite errors. Both Lagrangian methods, however, compute large overshoots in the postshock value. The higher-order Godunov method is best at computing the contact discontinuity, while the Lagrange plus remap scheme is more successful than the two Lagrangian methods. The two Eulerian methods both com-

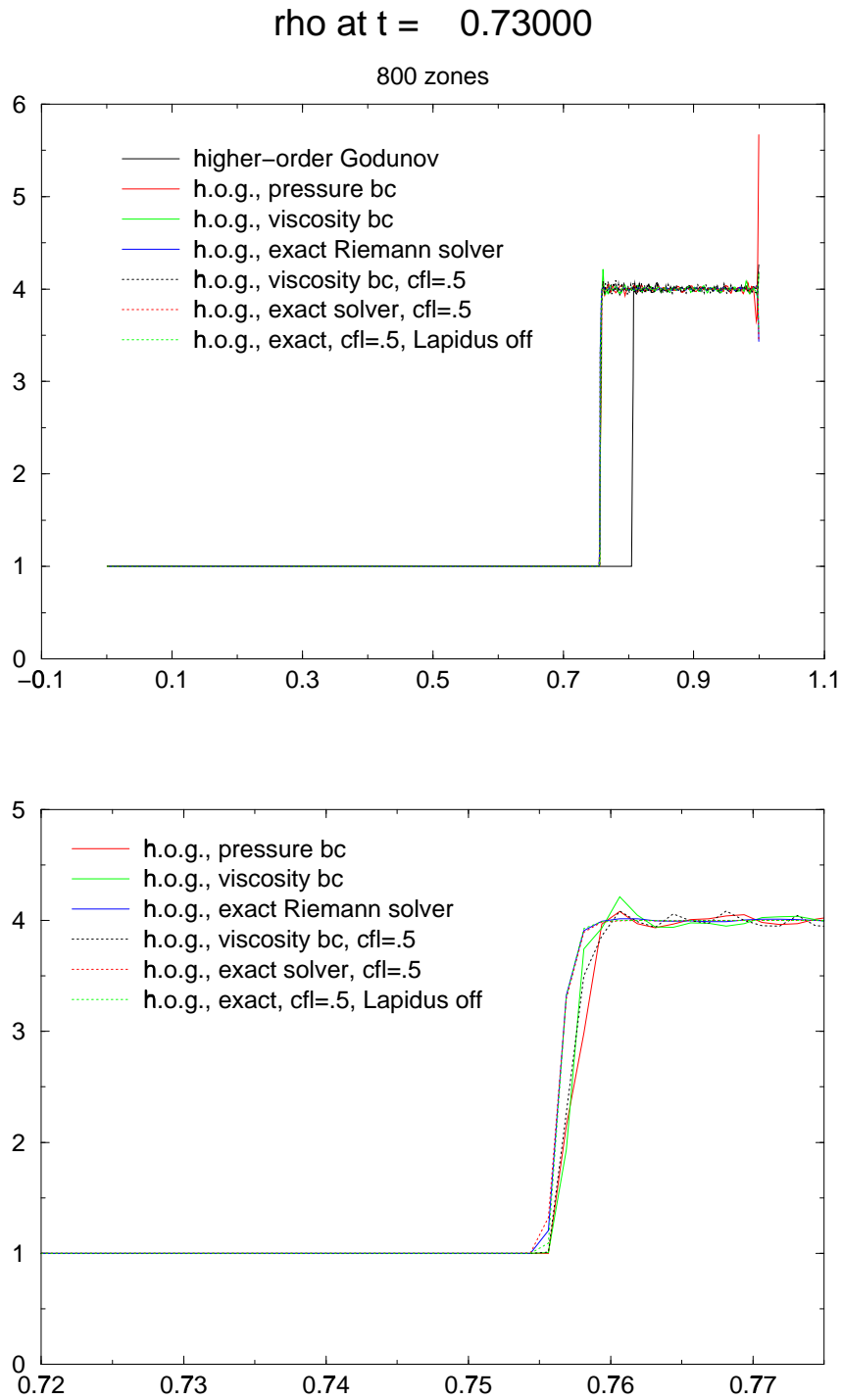


Figure 17: Density at $t = 6$ for the planar Noh problem at $t = .73$ on a grid of 800 zones. Higher-order Godunov results are shown only. The full problem domain and a closeup of the shock region are shown.

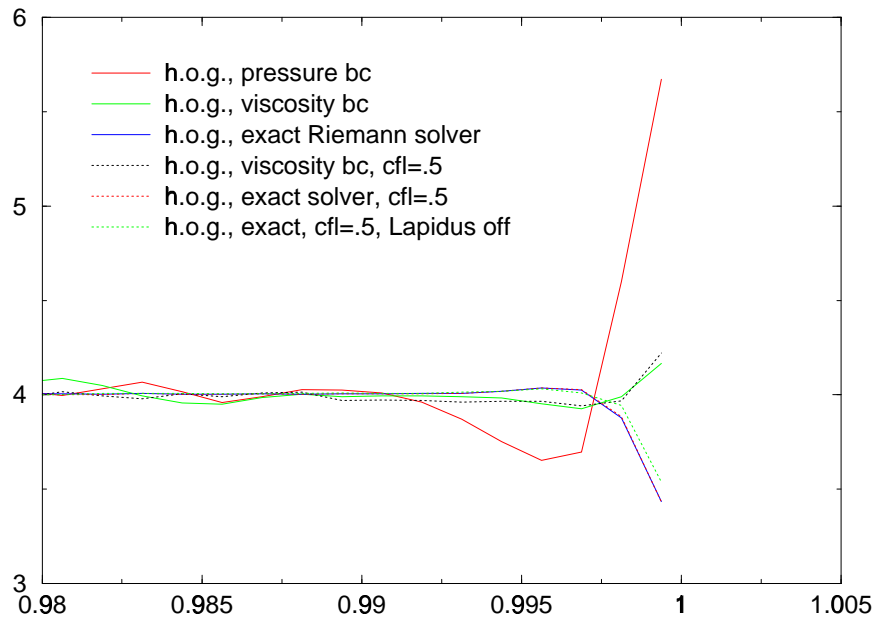
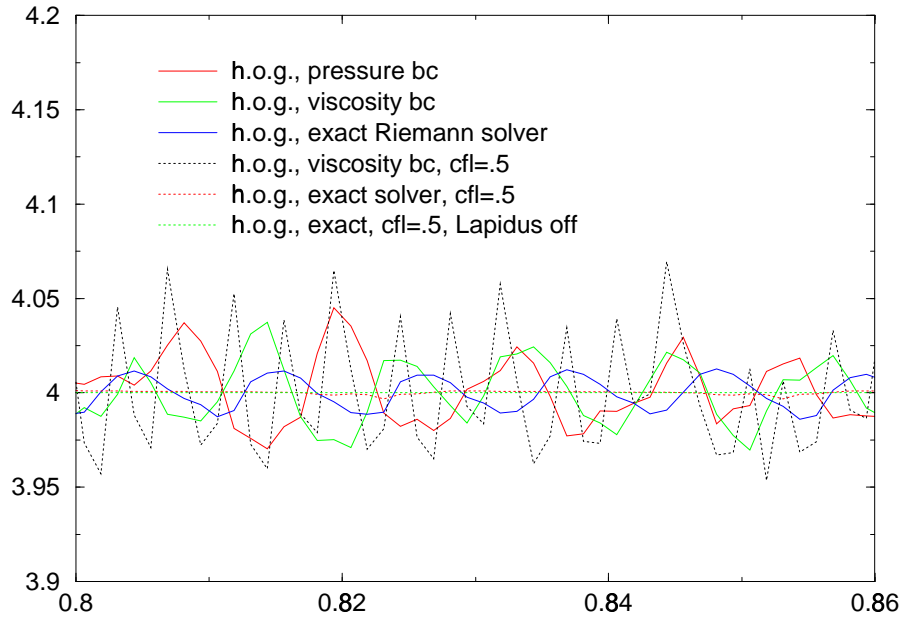


Figure 18: Density at $t = 6$ for the planar Noh problem at $t = .73$ on a grid of 800 zones. Higher-order Godunov results are shown only. Closeups of the postshock and near wall regions are shown.

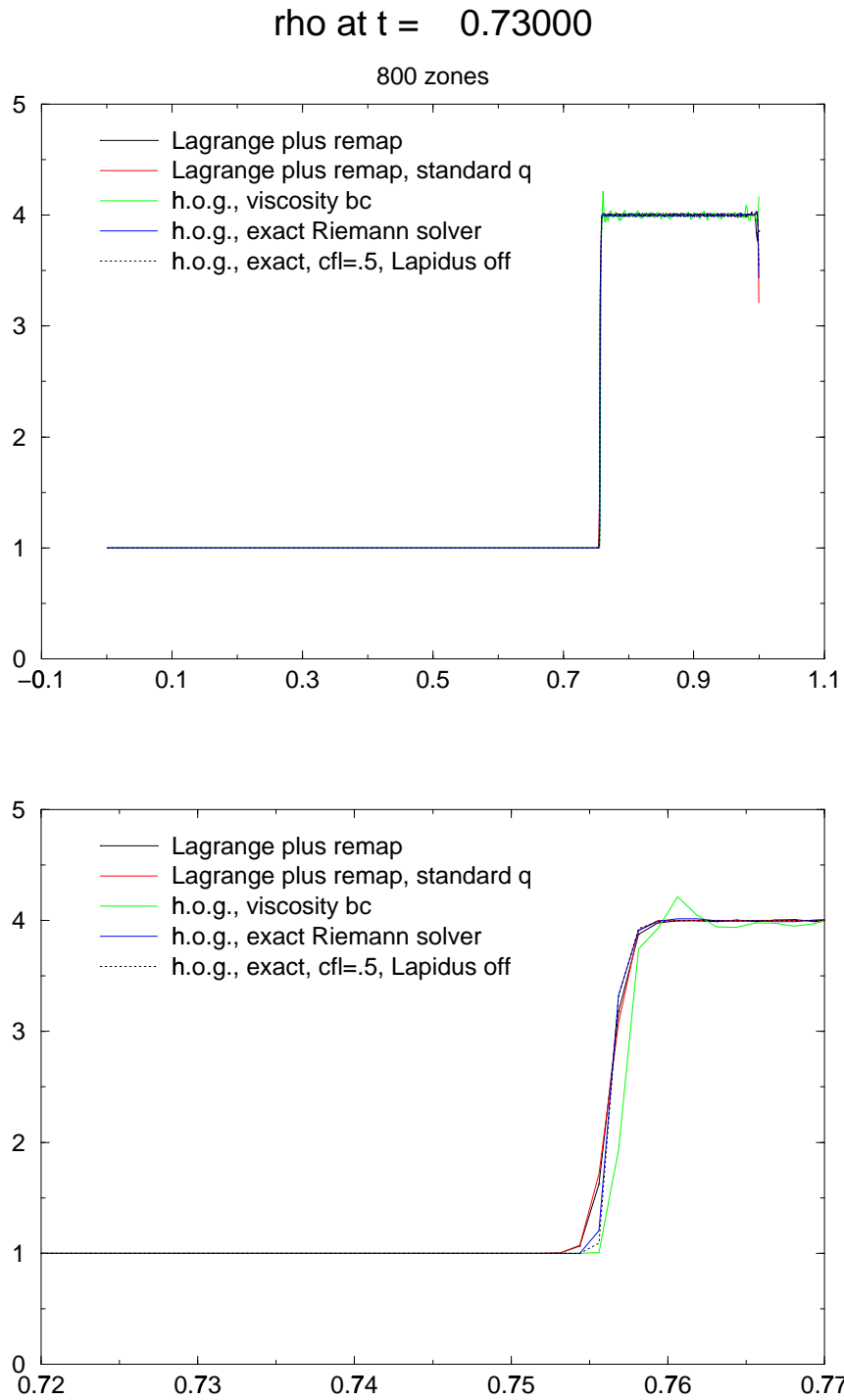


Figure 19: Density at $t = 6$ for the planar Noh problem at $t = .73$ on a grid of 800 zones. Lagrange plus remap and higher-order Godunov results are shown. The full problem domain and a closeup of the shock region are shown.

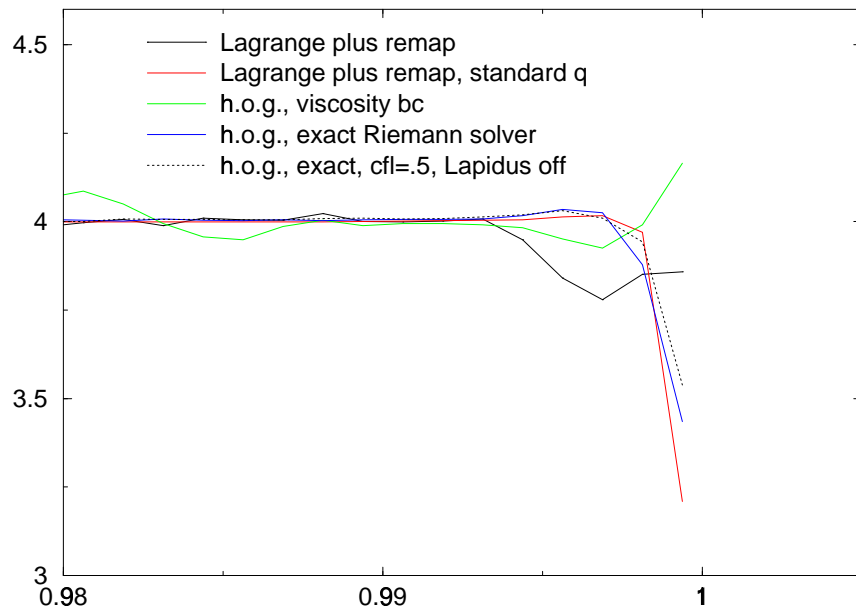
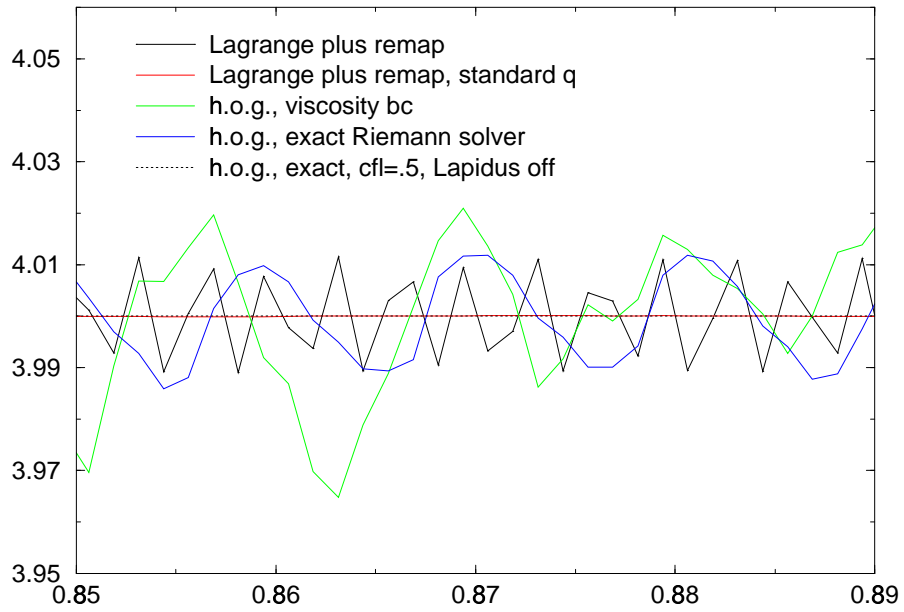


Figure 20: Density at $t = 6$ for the planar Noh problem at $t = .73$ on a grid of 800 zones. Lagrange plus remap and higher-order Godunov results are shown. Closeups of the postshock and near wall regions are shown.

pute overshoots at the contact, the higher-order Godunov method the least, while the two Lagrangian methods show large oscillations there. On the 1440 zone grid, the higher-order Godunov results best match the exact solution, although they do slightly underestimate the speed of the shock and show a small undershoot at the contact discontinuity. The Lagrange plus remap scheme and the staggered grid Lagrange scheme both slightly overestimate the speed of the shock. The Lagrange plus remap scheme computes a large but relatively narrow overshoot in the density at contact discontinuity. The staggered grid Lagrange scheme spreads this overshoot over a wider region. The higher-order Godunov Lagrange scheme shows the worse results. It overestimates the speed of the shock and spreads the overshoot at the contact over the entire region between the contact and the shock.

Discussion, conclusions, and future work

The results in the previous section demonstrate that a staggered grid, Lagrange plus remap, artificial viscosity scheme can compute results for Eulerian shock hydrodynamics that are comparable to those of a cell centered, direct Eulerian, higher order Godunov method. Moreover, they show that certain features of the current Lagrange plus remap scheme contribute to its improved performance relative the method examined by Woodward and Colella (1984). Three critical features in particular are the use of the monotonic artificial viscosity in the Lagrange step and the use of a van Leer (or comparable) limiter in conjunction with the separate advection of internal and kinetic energies in the remap step.

Additional considerations appear to be important in the calculation of flows with shear instabilities. Of the three problems examined by Woodward and Colella (1984) the double Mach reflection problem is the only such flow. The results there, however, do not show the rollups induced by a Kelvin-Helmholtz instability in the first contact discontinuity or the wall jet because the calculation is not adequately resolved. In this paper we examined two such flows, the shock reflection as well as the shock refraction problems, at sufficient resolution to see the Kelvin-Helmholtz instability. In the case of the reflection problem, we saw that the instability was nearly completely suppressed if the hourglass filter was used in the Lagrange step and partially suppressed if a spatially split advection scheme was used in the remap step. We suspect that the hourglass filter may damp physical as well as spurious numerical vorticity, while the split advection scheme may introduce extra numerical dissipation. On the other hand, for the refraction problem we saw no such suppression with the split remap and only moderate suppression with the hourglass filter. We also saw for the reflection problem that using milder filtering of the hourglass modes resulted in less suppression of the interface rollups. These results are not definitive; in particular, the split advection scheme used here is only one of a number of possible implementations. Nevertheless, they do suggest that one should exercise caution in the use of hourglass filters and split advection schemes for problems in which shear instabilities are important.

The results for several of the test problems warrant additional discussion. The interacting blast wave results suggest that at least in problems with strong shocks it is necessary to fully conserve in the vicinity of the shock in order to capture the correct shock speed, although it is not necessary in smooth regions of the flow. They also demonstrate that in some cases the Lagrange plus remap approach can resolve contact discontinuities much better than the higher-order Godunov approach. The double Mach reflection results show that some time-centering details of the predictor-corrector formulation in the Lagrange step are not overly

LeBlanc shock tube: e at t = 6.0

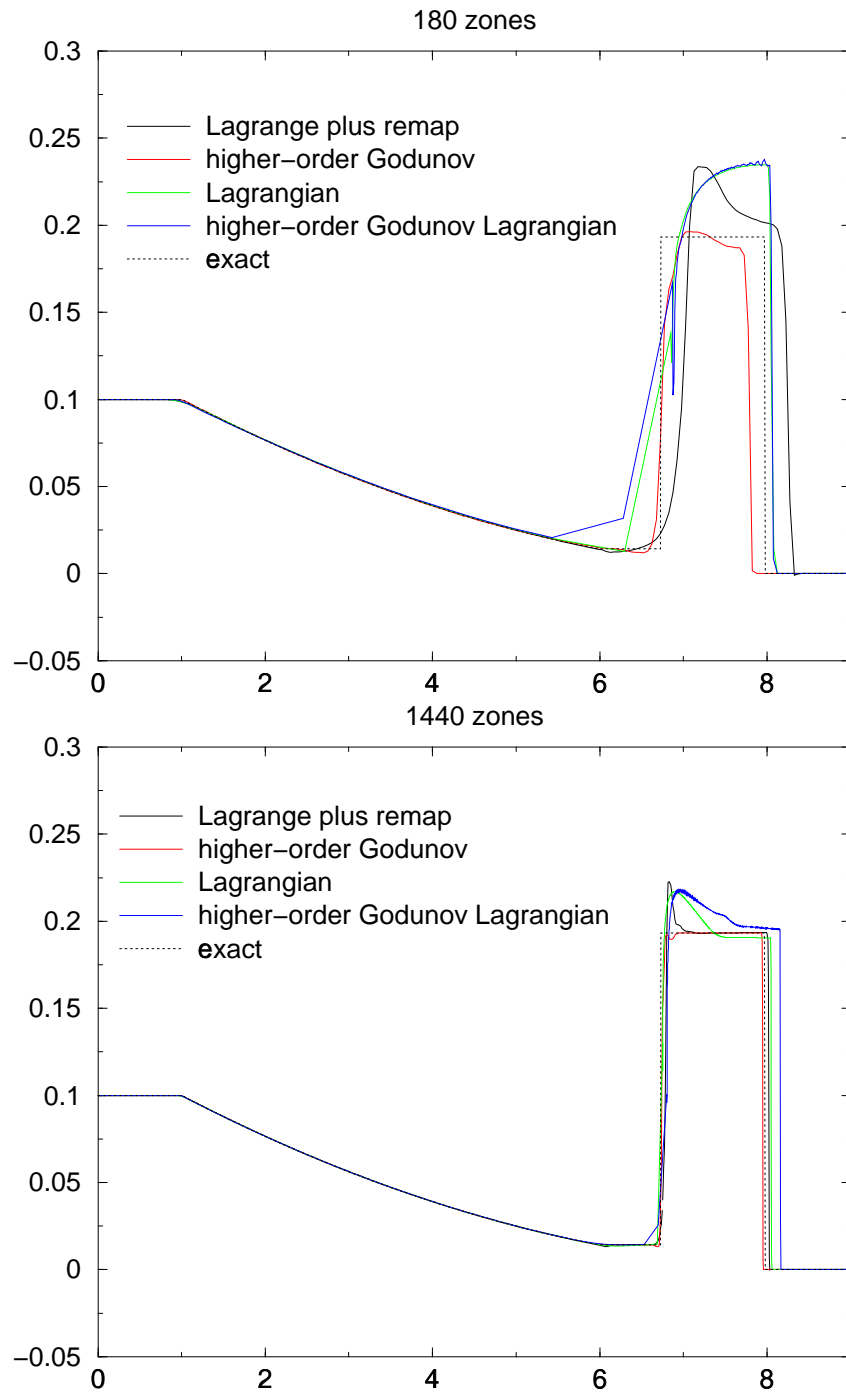


Figure 21: Internal energy at $t = 6$ for the LeBlanc shock tube on grids of 180 and 1440 zones.

LeBlanc shock tube: e at t = 6.0

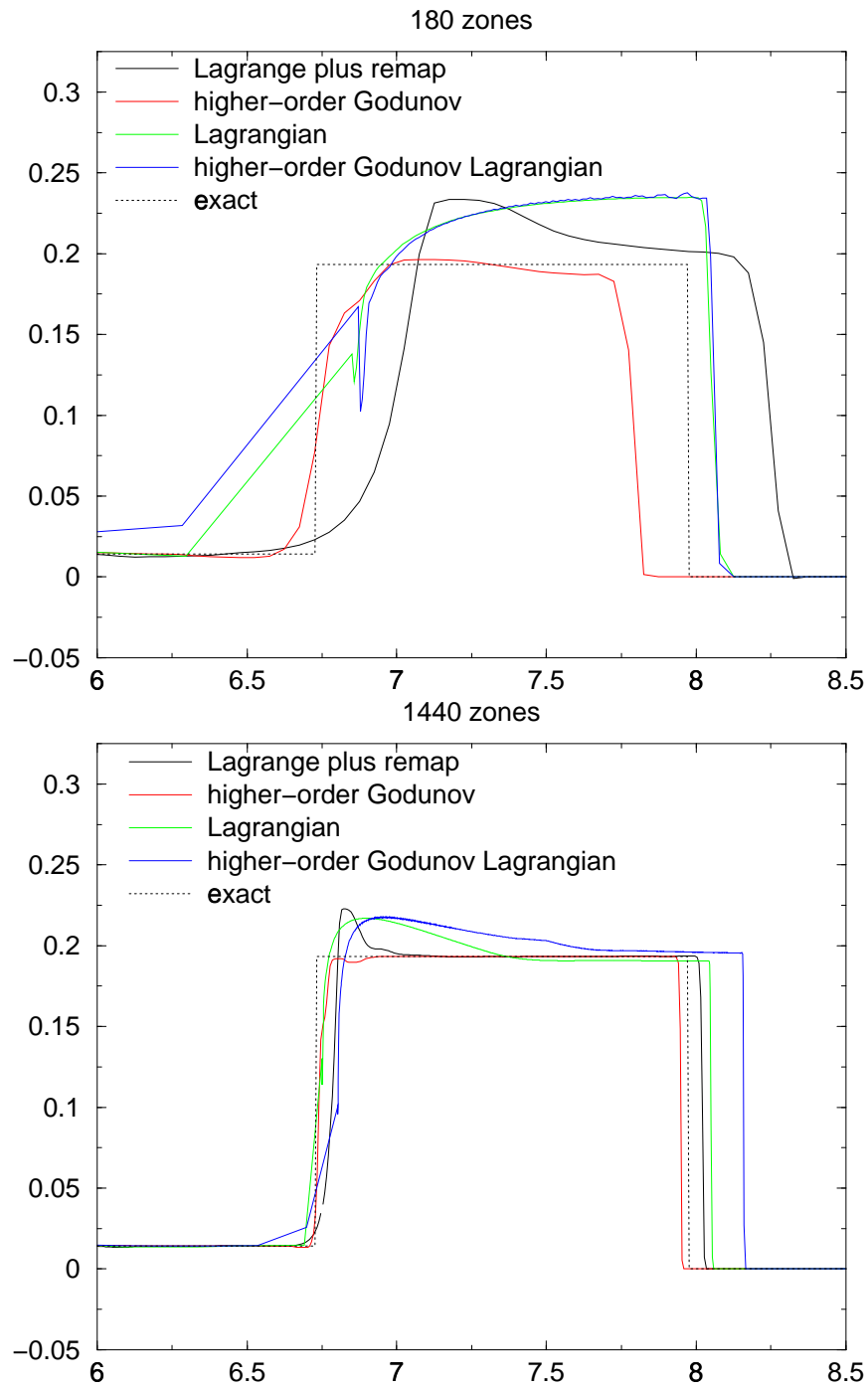


Figure 22: Internal energy at $t = 6$ for the LeBlanc shock tube on grids of 180 and 1440 zones. Closeup of results shown in Figure 21.

critical, at least in the context of gas dynamics. The shock refraction problem results are somewhat inconclusive. They do show that the Lagrange plus remap and the higher-order Godunov algorithms can compute similar results for refractions of the MRR type for strong incident shocks at fast-slow gas interfaces. The relative differences of the results seen near the triple point are significant, however, and require further investigation. The Noh problem computations are interesting in that the Lagrange plus remap scheme produced accurate results without any algorithmic adjustments while the higher-order Godunov scheme did require modifications, albeit relatively simple ones. The LeBlanc problem, on the other hand, is the one problem for which the Lagrange plus remap scheme did not fare as well as the higher-order Godunov method. The problems experienced by our Lagrange plus remap scheme, in particular the density overshoots at the contact discontinuity, do seem to originate in the Lagrange step. Moreover, at least for the two shock capturing methodologies we are considering, these problems are independent of the numerical approach. Specifically, difficulties stemming from a failure to adequately mass match the zoning can be seen in a pure Lagrangian calculation regardless of whether an artificial viscosity or a Godunov approach is used for shock capturing. Conversely, it is the direct Eulerian approach, and not the higher-order Godunov methodology itself, that enables the direct Eulerian Godunov scheme here to compute accurate results for the LeBlanc problem.

The work in this paper was done in conjunction with the research and development of a structured grid local adaptive mesh refinement scheme (Berger and Colella, 1989) suitable for use with a staggered grid ALE methodology. Part of this work will entail implementation of the Lagrange plus remap algorithm in two-dimensional cylindrical coordinates as well as in three-dimensions. As that development proceeds, we will further our comparison of higher-order Godunov and staggered grid Lagrange plus remap schemes. We will also further the comparison to problems with interface instabilities other than those of the Kelvin-Helmholtz type.

Acknowledgments

This work was performed under the auspices of the U.S. Department of Energy by University of California Lawrence Livermore National Laboratory under contract No. W-7405-Eng-48. The codes implementing the algorithms described in this paper were developed using SAMRAI (Hornung and Kohn, 1997), an object-oriented framework for the development of structured grid adaptive mesh refinement applications. The two-dimensional plots were generated using the Overture package (Brown *et al.*, 1998). We thank Rich Hornung, Scott Kohn, and Noah Elliot for their help with SAMRAI, Bill Henshaw for his help with Overture, Bob Tipton for helpful discussions, Jeff Greenough for suggesting and discussing the shock refraction problem, and Kyle Chand for providing an exact solution to the Sedov problem.

References

- Abd-El-Fattah, A.M., and Henderson, L.F., “Shock waves at a fast-slow interface,” *J. Fluid. Mech.*, **86**, 15–32 (1978).
- Bell, J.B., Colella, P., and Trangenstein, J., “Higher order Godunov methods for general systems of hyperbolic conservation laws,” *J. Comput. Phys.*, **82**, 362–397 (1989).
- Bell, J.B., Colella, P., Trangenstein, J.A., and Welcome, M., “Adaptive mesh refinement on

- moving quadrilateral grids,” in *Proceedings, AIAA 9th Computational Fluid Dynamics Conference*, Buffalo, New York, June 14-16, 1989, p. 471-579.
- Benson, B.J., “Computational methods in Lagrangian and Eulerian hydrocodes,” *Comp. Meth. Appl. Mech. Eng.*, **99**, 235–394 (1992).
- Benson, B.J., “Momentum advection on a staggered mesh,” *J. Comput. Phys.*, **100**, 143–162 (1992a).
- Berger, M.J., and Colella, P., “Local adaptive mesh refinement for shock hydrodynamics,” *J. Comput. Phys.*, **82**, 64–84 (1989).
- Brown, D.L., Henshaw, W.D., and Quinlan, D.J., *Overture: An object-oriented framework for solving partial differential equations on overlapping grids*, Lawrence Livermore National Laboratory, Livermore, CA, UCRL-JC-13201 (1999).
- Christensen, R.B., *Godunov methods on a staggered mesh — an improved artificial viscosity*, Lawrence Livermore National Laboratory, Livermore, CA, UCRL-JC-105269 (1990).
- Colella, P., “A direct Eulerian MUSCL scheme for gas dynamics,” *SIAM J. Sci. Stat. Comput.*, **6**, 104–117 (1985).
- Colella, P., “Multidimensional upwind methods for hyperbolic conservation laws,” *J. Comput. Phys.*, **87**, 171–200 (1990).
- Colella, P., Lawrence Berkeley National Laboratory, Berkeley, CA, private communication (2000).
- Colella, P., Glaz, H.M., and Ferguson, R.E., unpublished report (1993).
- Colella, P. and Puckett, E.G., *Finite Difference Methods for Computational Fluid Dynamic*, (Cambridge University Press, to be published). Also available as ftp://math.ucdavis.edu/pub/users/egp/Colella_and_Puckett/.
- Colella, P., and Woodward, P.R., “The piecewise parabolic method (PPM) for gas-dynamical simulations,” *J. Comput. Phys.*, **54**, 174–201 (1984).
- Crandall, M.G., and Majda, A., “The method of fractional steps for conservation laws,” *Numer. Math.*, **34**, 284–314 (1980).
- Darlington, R.M., McAbee, T.L., and Rodrigue, G., “A study of ALE simulations of Rayleigh-Taylor instability,” *Comp. Phys. Comm.*, submitted. Also appears as Lawrence Livermore National Laboratory, Livermore, CA, UCRL-JC-135634, Rev. 1 (1999).
- Glaz, H.M., Colella, O., Glass, I.I., and Deschambault, R.L., “A numerical study of oblique-shock wave reflections with experimental comparisons,” *Proc. Royal Soc. London A*, **398**, 117–140 (1985).
- Greenough, J.A., Lawrence Livermore National Laboratory, Livermore, CA, private communication (2000).
- Henderson, L.F., and Puckett, E.G., “Anomalous refraction of shock waves in materials with general equations of state. Part I. The shock pair system,” *Trans. Royal Soc. London A*, submitted (1993).
- Hirt, C.W., Amsden, A.A., and Cook, J.L. “An arbitrary Lagrangian-Eulerian computing method for all flow speeds,” *J. Comput. Phys.*, **14**, 227–253 (1974).
- Hornung, R.D., and Kohn, S.R., *Future directions for adaptive mesh refinement in ASCI and other LLNL simulation projects*, Lawrence Livermore National Laboratory, UCRL-ID-12833 (1997).
- Jun, B.I., *A simple advection scheme for material interface*, Lawrence Livermore National Laboratory, Livermore, CA, UCRL-JC-139912 (2000).

- Landshoff, R., *A numerical method for treating fluid flow in the presence of shocks*, Los Alamos National Laboratory, Los Alamos, NM, LA-1930 (1955).
- LeBlanc, J., Lawrence Livermore National Laboratory.
- Margolin, L.G., and Pyun, J.J., *A method for treating hourglass patterns*, Los Alamos National Laboratory, Los Alamos, LA-UR-87-439 (1987).
- Miller, G.H., and Puckett, E.G., “A high-order Godunov method for multiple condensed phases,” *J. Comput. Phys.*, **128**, 134–164 (1996)
- Noh, W.F., Lawrence Livermore National Laboratory, Livermore, CA, unpublished report, 1956.
- Noh, W.F., “Errors for calculations of strong shocks using an artificial viscosity and an artificial heat flux,” *J. Comput. Phys.*, **72**, 78–120 (1987).
- Pember, R.B., Bell, J.B., Colella, P., Crutchfield, W.Y., and Welcome, M.L., “An adaptive Cartesian grid method for unsteady compressible flow in complex geometries,” *J. Comput. Phys.*, **120**, 278–304 (1995).
- Pember, R.B., Greenough, J.A., and Colella, P., *An adaptive, higher-order Godunov method for gas dynamics in three dimensional orthogonal curvilinear coordinates*, Lawrence Livermore National Laboratory, Livermore, CA, UCRL-JC-123351 (1996).
- Peterkin, R.E., Frese, M.H., and Sovinc, C.R., “Transport of magnetic flux in an arbitrary coordinate ALE code,” *J. Comput. Phys.*, **140**, 148–171 (1998).
- Roe, P.L., “Approximate Riemann solvers, parameter vectors, and difference schemes,” *J. Comput. Phys.*, **43**, 357–372 (1981).
- Saltzman, J.S., and Colella, P., *Second order corner coupled upwind transport methods for Lagrangian hydrodynamics*, Los Alamos National Laboratory, Los Alamos, NM, LA-UR-85-678 (1985).
- Sedov, L.I., *Similarity and Dimensional Methods in Mechanics*, (Academic Press, New York, 1959).
- Shestakov, A.L., Prasad, M.K., Milovich, J.L., Gentile, N.A., Painter, J.F., Furnish, G.M., and Dubois, P.F., “The ICF3D code,” *Comp. Meth. Appl. Mech. Eng.*, **187**, 181–201 (2000).
- Smith, R.W., “AUSM(ALE): A geometrically conservative arbitrary Lagrangian-Eulerian flux splitting scheme,” *J. Comput. Phys.*, **150**, 268–286 (1999).
- Strang, G., “On the construction and comparison of difference schemes,” *SIAM J. Numer. Anal.*, **5**, 506–517 (1968).
- Tipton, R.E., Lawrence Livermore National Laboratory, Livermore, CA, unpublished report (1990).
- van Leer, B., “Towards the ultimate conservative difference scheme. V. A second-order sequel to Godunov’s method,” *J. Comput. Phys.*, **32**, 101–136 (1979).
- Wilkins, M.L., “Calculation of elastic-plastic flow,” *Meth. Comp. Phys.*, **3**, 211–263 (1964).
- Wilkins, M.L., *Computer Simulation of Dynamics Phenomena* (Springer-Verlag, New York, 1999).
- Woodward, P.R., and Colella, P., “The numerical simulation of two-dimensional fluid flow with strong shocks,” *J. Comput. Phys.*, **54**, 115–173 (1984).

University of California
Lawrence Livermore National Laboratory
Technical Information Department
Livermore, CA 94551

